

POLITECNICO DI TORINO

*Master's Degree in  
Nanotechnologies for ICTs*

TESI DI LAUREA MAGISTRALE

---

**Carrier transport in nanostructured  
materials: a NEGF perspective on  
localization landscape**

---

*Candidate:*  
Andrea Marco CARIA

*Supervisor:*  
Prof. Francesco BERTAZZI  
Dr. Alberto TIBALDI  
Prof. Michele GOANO



December 2020



POLITECNICO DI TORINO

# *Abstract*

Dipartimento di Elettronica e Telecomunicazioni

Nanotechnologies for ICTs

## **Carrier transport in nanostructured materials: a NEGF perspective on localization landscape**

by Andrea Marco CARIA

The classic drift-diffusion model is not able to properly simulate structures like superlattices or quantum wells, because it does not take into account quantum effects such as tunneling or quantum confinement. The localization landscape theory is a clever mathematical tool that allows accounting quantum effects inside these types of devices, by replacing the original electrical potential with the effective quantum potential seen by carriers. This quantity is derived from the solution of a Schrödinger-type equation with an uniform right-hand side. Employing this theory, it is possible to predict the localization regions of carriers, their ground state energy, and their local density of states.

The localization landscape potential is used to determine the carrier densities, with the Fermi integral. Then, these latter results are introduced in the well-known Poisson equation, in order to develop a model capable of effectively introduce quantum effects. In order to prove the validity of this model, the outputs of the simulation are compared to the ones derived from an exact Poisson-Schrödinger solver, in which the quantum effects are perfectly modeled by the wave nature of the electrons and holes.

The localization landscape potential is introduced into a classical drift-diffusion solver to directly model carrier transport in a superlattice system. The obtained results are compared with the one found with a non-equilibrium Green's function (NEGF) approach, in which the scattering has been introduced by means of Büttiker probes, finding good agreement. This method is tested for several one-dimensional structures: quantum wells, ordered and disordered superlattices with different periodicity and distinct coupling factors.

The obtained results show particular agreement with the existing methods, especially for high coupled superlattices even when the disorder is introduced, which denote that the localization landscape method is an efficient tool for the development of devices based on quantum structures.



## *Acknowledgements*

I can not enough thanks to my supervisors for their continue support and assistance: Prof. Francesco Bertazzi, main supervisor; Dr. Alberto Tibaldi and Prof. Michele Goano, co-supervisors. I'm deeply indebted to my supervisors for the learning opportunity provided.

My accomplishment of this work would not have been done without my room mates, Mattia, Matteo and Alessandra that supported me during this endless quarantine. I would also like to express my gratitude to Francesco and Giovanna that give me some meaningful help in the final linguistic revisions of this work. I cannot begin to express my thanks to my friends, around the word, life without you is meaningless.

Finally, to my family and to my parents for their unfailing support in this five years, you give me the opportunity to make this life a wonderful adventure.



# Contents

<b>Abstract</b>	<b>iii</b>
<b>Acknowledgements</b>	<b>v</b>
<b>1 Introduction</b>	<b>1</b>
<b>2 Methods</b>	<b>5</b>
2.1 Schrödinger Model	5
2.1.1 Derivation of equations	7
2.1.2 Discretization in space	11
2.1.3 Density of states	15
2.2 Landscape Potential	17
2.2.1 The need of an effective potential	17
2.2.2 Landscape Potential	18
2.2.3 Eigenvalue estimates	20
2.2.4 Density of states and carrier densities	21
Integrated Density of State	22
2.2.5 Potential reference	23
2.3 Out-of-equilibrium	24
2.3.1 Description of the model	25
2.3.2 Moving to Landscape potential	26
2.4 NEGF and Buttiker probes	30
2.4.1 NEGF	31
2.4.2 Scattering	32
2.4.3 Fermi function	34
2.4.4 Equilibrium	34
2.4.5 Analytical integration of transversal wave-vector	36
2.5 Out-of-equilibrium	37
<b>3 Equilibrium simulations</b>	<b>39</b>
3.1 Quantum well	41
3.2 Superlattice	47
3.2.1 Periodic Superlattice	48
3.2.2 Disordered superlattice	54
3.2.3 NEGF simulations	57
<b>4 Out-of-equilibrium simulations</b>	<b>59</b>
4.1 Superlattice	60
4.2 Multiple-QW	67

<b>5 Conclusion</b>	<b>73</b>
---------------------	-----------

<b>A Numerical evaluation of NEGF Jacobian and Broyden iterative method</b>	<b>75</b>
---	-----------

# Chapter 1

## Introduction

In last years, infrared detection is used for an increasing number of applications, ranging from civil (measurement of body temperature for COVID-19 detection) to military purposes (night visors). Nowadays, the majority of these detectors are based on bulk mercury cadmium telluride HgCdTe (MCT) and InSb [1]. In particular the ones based on MCT are characterise by high quantum efficiency (>90%)[2] and moreover, they are also able to cover the whole IR spectral range, indeed the HgCdTe can be tailored for optimized detection in any region of the IR spectrum between 1 $\mu$ m and 25 $\mu$ m. These particular devices are used in wide range of applications, but they also exhibit some notable drawbacks especially in the mass production process. One of the main limitations of such devices is the operation temperature, for LWIR (long wave infrared) detection it has to be cooled to a temperature near the liquid nitrogen (77 K) while for the MWIR camera is enough to use the thermoelectric coolers by paying a small performance penalty. Moreover, the MCT detectors are affected by non-uniform growth defects and the substrate on which they are grown is CdZnTe, a very expensive and available in limited quantities alloy. A possible solution to this latter problem is to replace this exotic material substrate with a silicon one, but up to the latest researches, good performance has been limited to the MWIR band only. Finally, it has been seen that Hg has a high pressure vapour at the melting point of HgCdTe leading to the toxicity of material. It is for these reasons that in the lasts years a higher numbers of researches have been done to overcome the employment of such material in the IR photodetector. A promising solution is to use a periodic quantum structure, the superlattice. The most favourable ones are those based on III-V semiconductors, the modern state-of-arts on manufacturing processing allows to scale these devices for a high number of applications, for example, it enables to scale to large format FPAs with a high degree of spatial uniformity [2]. These devices are characterised by higher working temperature, higher sensitivity, lower weight and less manufacture costs.

Superlattices are a periodic system made by two or more materials, that usually have nearly the same lattice constant. These different materials are

deposited in a repetitive sequence of thin layers, the width of such layers are selected in order to give rise to quantum carriers confinement. Indeed, by shrinking the thickness of the layer the carriers do not behave as free particles anymore but a purely quantum confinement effect arises in the regions with lower potential (wells). Moreover, when the carriers de Broglie wavelength becomes comparable to the barrier thickness of the superlattice, the wave functions of the confined carriers in the wells tend to overlap due to tunnelling. This overlap between contiguous layers results in the development of minibands in the conduction and valence band. According to in which part of the device the electrons and holes are confined, it is possible to classify semiconductor into three types, that sorting can be also defined on how the valence and conduction band of the two material align when they are put into contact. If the electron and holes are confined within the same layer of material it is possible to talk about a type-I superlattice while if the electrons are confined in a different layer with respect to the holes the superlattice is defined as type-II. Moreover, on this latter type, further classification can be made by considering the edge of conduction and valence band of the two materials, as an example, if both the valence and the conduction band edges of the second material are above the band edges of the first material, it is called a broken type-II band alignment. For detection application both the type-I [3] and type-II [4] can be used but the latter shows more promising results and application while the first one can be also used to develop tunable Brag reflection gratings [5]. In those superlattices the detection of an incoming photon is done when an electron-hole pair is excited from a lower energy miniband to a higher one, those minibands can be in the same band or in two distinct ones (conduction and valence). So in order to properly describes this kind of device it is fundamental to determine the background carrier concentrations and to derive the minority carriers' lifetimes and their diffusion length. Unfortunately, the quantum effects that give rise to the carriers confinement introduces in the modelling a further complexity.

Accounting for carrier localization induced by two semiconductor's heterojunction is a daunting task. A proper description of such structure usually requires solving the Schrödinger equation to obtain the carrier distributions, or applying a nonequilibrium Green's function (NEGF) to describe the behaviour of carrier quantum transport. Unfortunately, both these techniques are very time consuming for multidimensional devices, so a new method that allows to describe the carriers and their motion with a low computational time is needed.

One of the earliest solutions was to use the classical drift-diffusion(DD) model, but its main limitation is the inability to simulate the carrier transport in a superlattice system directly because due to quantum effects, the actual potential seen by electrons(holes) in a superlattice system is different from the original potential of the classical Poisson-DD model. If the band structure of a superlattice was put directly into the classical Poisson-DD solver, it would behave like a multibarrier where carrier transport might be forbidden. However, the models based on the iterative solution of both Poisson and drift-diffusion

equations have the main advantage to be fast enough to simulate a multi-dimensional device. The quantum effects can be introduced in such models by replacing the potential distribution with an effective one, that introduced in the classical DD solver, allows to simulate the superlattice system directly. According to how this potential is defined, different models can be implemented.

One of the first definitions of such potential was given by Bohm in 1952 [6], however, this potential was calculated by solving the Schrödinger leading to an high computation cost. One of the most promising definitions of such potential is the relatively recent localization landscape (LL) theory, proposed by Filoche and Mayboroda, in 2012 [7]. The main idea of this method is to calculate the effective potential, not from the computation expensive eigenvalue Schrödinger equation, but from a second-order differential equation derived from a modified version of the Schrödinger one. By doing so small simulation time is achieved even for high dimensional structures. In past years, this theory was benchmarked with the Poisson-Schrödinger solver for different quantum structures with the aim to predict the Anderson localization due to disorder, [8], showing appealing results. Later on, in 2020 this method was used to simulate the carriers transport in a type II superlattice InAs/InAsSb [9], obtain, even for that case, promising outputs.

In this work, the landscape model was tested for some well-known 1-dimensional quantum structures, like quantum wells or type-I superlattices. Moreover the position disorder has been introduced in a selected set of structures, to understand how it changes the fundamental device property of a photodetector [10] and if the landscape potential properly described this deviation from the ideality. These results have been compared to the one obtained with a Poisson-Schrödinger solver, for the what concerns the equilibrium simulation, while for out-of-equilibrium simulation the results have been confronted with the ones obtained with the non-equilibrium Green's function approach in which the scattering has been introduced through the Büttiker probes [11].

After a brief presentation and description of the models used, the results are presented in two main sections, one for equilibrium simulations while the other is devoted to the modelling of structures out of equilibrium. For what concerns the first case, two types of structures are considered, a quantum well (QW) and a superlattice. This theory was applied to a QW in order to give a first validity-check at different confinement potential, these results have been compared to both the NEGF approach and the Schrödinger solver. Then, type-I superlattices have been studied, ranging from high coupled structures to low coupled ones (multiple-QW). Even for those cases, the obtained results are benchmarked with the NEGF and Schrödinger methods, moreover, a fictitious depositional error has been introduced to describe the not perfectly periodic SL, for this latter analysis only two meaningful structures have been simulated.

Finally, the last chapter of results presentation is devoted to the implementation of localization landscape theory out of equilibrium, for this study only the superlattice systems have been considered. On those structures a small bias has been applied with the aim to derive the current density and other meaningful quantities, then all these outputs have been compared to the results obtained with the NEGF approach, showing some interesting comparison.

Both quantum wells and the superlattice systems are based on the Al-GaAs/GaAs hetero-junction, which leads to a type-I structure. Nowadays, those devices based on such materials are not so common in the market because it is preferable to use type-II superlattice at least for detection purpose, while type-I superlattices are more common in Bragg-grating reflectors. The reason why not so innovative alloys were taken, is that this study is a preliminary validation of the model, especially out of equilibrium, by considering these well-known materials all the possible errors derived from the not perfect model of the material are removed from the implementation allowing to understand the true strength of this model.

## Chapter 2

# Methods

In this chapter, a theoretical description of the implemented methods has been provided for all the models and equations used, in particular for the latter a concise presentation has been given underling the main aspects and approximations performed. Moreover, for some meaningful equations, a brief mathematical derivation has been supplied.

As a first step, the Schrödinger model has been described starting from the discretization of the one-dimensional Schrödinger equation. This implementation has been very useful to provide a term of comparison for the equilibrium simulations, that have been made by introducing the Landscape potential. Then, this above-mentioned landscape potential has been introduced, with a brief mathematical description, and then implemented with the Poisson equation in order to achieve the wanted landscape-Poisson solver. Moreover, this theory has been introduced in a drift-diffusion model with the aim to study structures even out of equilibrium.

### 2.1 Schrödinger Model

As the first step, the one-dimensional Schrödinger equation has to be derived and then discretized in space in order to be able to calculate the carrier densities for a one dimensional device, later on, this charge distribution has been introduced in the Poisson equation leading to the Poisson-Schrödinger solver.

The Schrödinger equation is a linear partial differential equation that resolved allows obtaining a set of wave-functions  $\psi_n$  that, with their associated eigenvalues  $E_n$ , properly describe the electrical properties of the system in study. Given a potential shape  $\phi$  is possible to solve this equation by obtaining the above-mentioned physical quantities from which is possible to calculate the electrons and holes concentration in conduction and valence band, respectively. Therefore, by introducing the activated dopants density and merging all together is possible to obtain the net charge density ( $\rho$ ), that

has to be introduced in the Poisson equation to obtain the equilibrium potential shape. The basic idea of this solver is to derive the potential distribution  $\phi(z)$  and their associated charge density  $\rho(z)$ , by solving respectively the Poisson and Schrödinger equations. Unfortunately, these two quantities are mutually dependent, an iterative method has to be implemented to achieve a stable solution. By solving the Schrödinger equation is possible to determine the carrier densities from which the net charge  $\rho$  is calculated. This quantity is the main input of the Poisson equation that allows determining the potential shape  $\phi$ , however this new shape of potential, introduced inside the Schrödinger equation, changes the electrons and holes distributions, they further transform the charge density and the potential. It is easy to see the importance to select a proper initial guess of  $\phi_0$  to be able to reach the convergence of results, an improper choice of the initial potential guess can lead to an unphysical distribution of the carriers at the first loop and so bring the solver hopelessly to far from the solution preventing convergence from being achieved.

This iterative method proceeds until the variation of potential, due to the new charge density, is lower than a certain threshold.

In fig.(2.1) has been depicted a schematic flowchart that summarizes all the steps described above, adding some important considerations and all the derived equations, which have been described in the following sections. As soon as the convergence is reached, it is possible to extrapolate further results, such as the density of state or ground state energy.

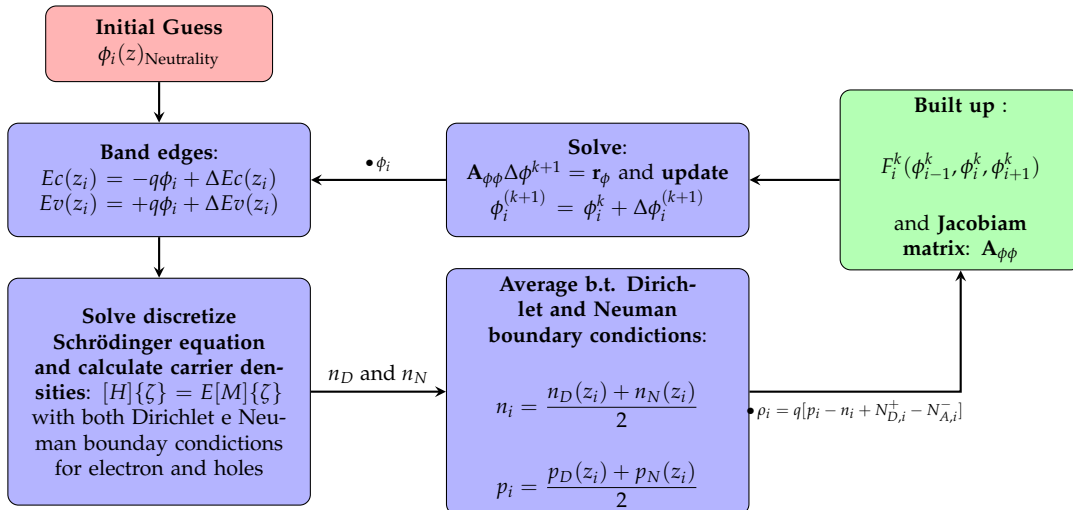


FIGURE 2.1: Poisson-Schrödinger flowchart

### 2.1.1 Derivation of equations

As the first step in the description of the model, the Schrödinger equation has to be defined. In this master thesis, all the devices in the study have been considered as one-dimensional structure. Therefore, a generic one dimensional confining potential  $V$  is considered, it depends only on the coordinate  $z$  and the associated Schrödinger equation is written as:

$$\left[ -\frac{\hbar^2}{2m^*} \nabla^2 + V(\vec{z}) \right] \psi(\vec{r}) = E\psi(\vec{r}) \quad (2.1)$$

This is a 3D partial differential equation, but considering the fact that particles are free to move along the  $x$  e  $y$  direction the searched wave-function  $\psi$  can be decomposed as:

$$\psi_m(\vec{k}, \vec{r}) = \psi_m(k_x, k_y, x, y, z) = C e^{ik_x x} e^{ik_y y} \zeta_m(\vec{k}, z) \quad (2.2)$$

where the wave-vector  $\vec{k}$  depends only on  $x$  and  $y$  coordinates since the third component along  $z$  direction labelled as  $k_z$  has being quantized due to the external confining potential and it has been substituted by an integer number  $m$ . On the other hand, along the transversal pathway particles are not submitted to any potential and their motion is described as a travelling plane wave. So the three-dimensional wave-function can be seen as a product of two well-known plane waves along the  $x$  and  $y$  coordinate and a set of unknown wave-function  $\zeta_m$  along the  $z$  direction.

The equation (2.2), if properly normalized, provides information on probability of the particle to be in a certain position  $(x, y, z)$  and to have a certain momentum  $(k_x, k_y, k_z)$ , recalling the fact that due to the potential  $V(z)$  the latter component of wave vector have been discretized, the eq.(2.1) can be written as:

$$\left[ -\frac{\hbar^2}{2m^*(z)} \frac{\partial^2}{\partial z^2} + \frac{\hbar^2 k_x^2}{2m^*(z)} + \frac{\hbar^2 k_y^2}{2m^*(z)} + V(\vec{z}) \right] \zeta_m(\vec{k}, z) = E_m(\vec{k}) \zeta_m(\vec{k}, z) \quad (2.3)$$

Under this formalism the eq.(2.3) should be resolved for each wave-vector  $\vec{k}$ . In order to obtain the carrier densities a *counting* problem has to be solved, as it done in eq.(2.2) it is possible to separate the contribute of transversal  $(x, y)$  and perpendicular plane  $(z)$ . For what concerns the latter direction eq.(2.3) can be solved by fixing a  $\vec{k}$  value, then with a numerical tool is possible to obtain the  $\zeta_m$  wave-functions and their associated eigenvalues that describe the confinement along  $z$  direction, from this discrete number of eigenvalues is possible to calculate the carrier densities.

The calculation becomes more complicated when the transversal plane  $(x, y)$

is taken into consideration. In fact, the wave-vectors have a continuous domain because due to open boundary no confinement effect arises. Regretfully, this *continuous nature* of wave-vector does not allow to solve the Schrödinger equation, and so it is impossible to obtain a finite number of eigenvalues needed for the calculation of the electron density.

An important step forward can be performed by introducing a boundary domain on both  $x$  and  $y$  directions, this has two main effects: first of all, it allows to define an area of normalization in such a way that the  $|\psi_m|^2$  defined in (2.2) can be viewed as a probability density, secondly, it leads to a quantization of the wave-vector  $\vec{k}$  along the transversal direction. So, if the confinement is introduced also on the transversal direction by means of a box of length  $L_x$  and width  $L_y$  and the periodic boundary condition (Born-von-Karman) are imposed, the component of  $\vec{k}$  can be written as:

$$k_x = n_1 \frac{2\pi}{L_x} \quad \text{and} \quad k_y = n_2 \frac{2\pi}{L_y} \quad (2.4)$$

where  $n_1$  and  $n_2$  are integer numbers that describe quantization state.

A sketch that can help to better visualise this mathematical trick is depicted

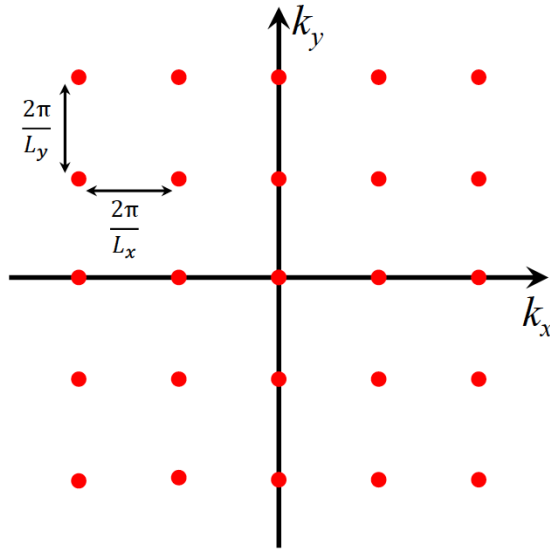


FIGURE 2.2: Discretized transverse  $\vec{k}$  space

fig.2.2, taken from [12], where each of the red points is all the possible momentum that an electron can assume. Two adjacent states are separated by a minimum distance equal to  $k_x$  or  $k_y$ , this means that it is possible to define an area equal to:

$$\frac{2\pi}{L_x} \cdot \frac{2\pi}{L_y} \quad (2.5)$$

where only one state is present. That definition allows to determine the factor  $C$  defined in eq.(2.2), by imposing:

$$\int_0^{L_x} dx \int_0^{L_y} dy \int_0^{L_z} dz |\psi_m(\vec{k}, x, y, z)|^2 = L_x \cdot L_y \int_0^{L_z} dz |C\zeta_m(\vec{k}, z)|^2 = 1 \quad (2.6)$$

It is straightforward to see that

$$C = \frac{1}{\sqrt{L_x \cdot L_y}} := \frac{1}{\sqrt{\mathcal{A}}} \quad (2.7)$$

Now, having imposed the normalization of the probability density, it is possible to calculate the electrons and holes densities, it is also important to notice that the  $|\psi_m|^2$  has the dimension  $1/m^3$  perfectly coherent for a density per unit of volume.

Finally, now that the probability density is known, the occupation probability for each states has to be introduced, the latter can be described by the *Fermi-Dirac distribution*:

$$f_{FD}(E, E_f) = \frac{1}{1 + \exp\left\{\left(\frac{E - E_f}{kBT}\right)\right\}} \quad (2.8)$$

this function has to be evaluated for each of the eigenvalue  $E_m$  coming from the eq.(2.3). By merging together all these considerations, it is possible to obtain the electron density by counting the state for unit volume. This procedure can be performed by summing over the total number of states the double integral of the probability function for each state (which is reduced to  $\zeta_m(\vec{k}, z)$  due to the absolute value squared), times the Fermi-Dirac distribution, over the number of states per k-space unit area ( $\mathcal{A}/2\pi$ ), obtaining:

$$n(z) = \frac{2}{(2\pi)^2} \sum_{m=1}^{N_{eig}} \int \int d\vec{k} |\zeta_m(\vec{k}, z)|^2 \cdot \frac{1}{1 + \exp\left\{\left(\frac{E - E_f}{kBT}\right)\right\}} \quad (2.9)$$

Two considerations have to be done on this formula: to start with a multiplication factor 2 is introduced in order to consider the effect of spin and Pauli exclusion principle that is not taken into account in the Schrödinger equation, secondly the area  $\mathcal{A}$  disappears from the calculations so, the arbitrary degrees of freedom introduced normalizing the wave-function and limiting the transversal domain, does not influence the final result.

A further simplification has to be performed before going on the implementation of the model, eq.(2.1) can be rewritten if the effective mass is taken as **axially invariant**, *i.e.* the band structure is equal for the radial direction. Within this approximation the component of wave-vector along  $x$  varies in the same way of  $k_y$ , therefore a *radius* in  $k$  space it can be defined as:  $k^2 = k_x^2 + k_y^2$  and the Schrödinger equation becomes:

$$\left[ -\frac{\hbar^2}{2m^*} \frac{\partial^2}{\partial z^2} + \frac{\hbar^2 k^2}{2m^*} + V(z) \right] \zeta_m(k, z) = E_m(k) \zeta_m(k, z) \quad (2.10)$$

where the obtained *eigenvalues* and *eigenfunctions* do not depend on the component of wave-vector but only on its magnitude.

Now, the integral in eq.(2.9) can be evaluated by writing  $k$  with polar quantities. By following the steps performed in [12] is possible to write an other, more *implementation-oriented* expression of the density of states:

$$n(z) = \frac{1}{\pi} \int k dk \sum_{m=1}^{N_{eig}} |\zeta_m(k, z)|^2 \cdot \frac{1}{1 + \exp\left\{\left(\frac{E-E_f}{k_B T}\right)\right\}} \quad (2.11)$$

This equation can be further rewritten introducing a discretization on  $k$  vector in order to perform the numerical integration as:

$$n(z) \simeq \frac{1}{\pi} \sum_{m=1}^{N_k} \sum_{m=1}^{N_{eig}} |\zeta_m(k, z)|^2 \cdot \frac{1}{1 + \exp\left\{\left(\frac{E-E_f}{k_B T}\right)\right\}} k_n \Delta k_n \quad (2.12)$$

Following the same steps done for electrons, the holes densities can be written as:

$$p(z) \simeq \frac{1}{\pi} \sum_{m=1}^{N_k} \sum_{m=1}^{N_{eig}^p} |\zeta_m^p(k, z)|^2 \cdot \frac{1}{1 + \exp\left\{\left(\frac{-E+E_f}{k_B T}\right)\right\}} k_n \Delta k_n \quad (2.13)$$

of course, the two Schrödinger eigenvalue problems have to be defined differently if electrons or holes are involved, the main differences are the effective mass parameter and the potential: conduction band for electron and valence for holes. The error introduced by this latter approximation it is negligible if the mesh step ( $\Delta k$ ), with which the vector  $k$  is discretized is small, in the limit of a number of mesh point ( $N_k$ ) equal to infinite the two formulas are the same.

It is important to recall that in eq.(2.12), the variation of the effective mass along the  $z$  direction is still taken into account within the wave-function  $\zeta_m$ ,

the only approximation that has been performed on the masses along the radial direction  $(x, y)$ .

### 2.1.2 Discretization in space

In order to be able to evaluate the Schrödinger eigen-problem with a calculator, a **discretization in space** has to be performed. Subspace  $z$  has been discretized into  $N_n$  node and  $N_n - 1$  element, furthermore, the dependence on transversal wave-vector  $k$  has been moved out the Schrödinger equation, it has been possible to do so, because the potential  $V$ , to which is subjected the quantum state, can be defined up to a constant value. It can be demonstrated that if the potential is shifted by a quantity  $K$  the obtained quantum states are also shifted by the same quantity. Taking this into account the eq.(2.1) can be rewritten as:

$$\left[ -\frac{\hbar^2}{2m^*} \frac{\partial^2}{\partial z_n^2} + V(z) \right] \zeta_m(k) = E_m \zeta_m(k) \quad (2.14)$$

then the dependency on the wave-vector  $k$  has been reintroduced on the found eigenvalues as:

$$E_m(k) = E_m + \frac{k^2 \hbar^2}{2m^*} \quad (2.15)$$

the term added to the obtained eigenvalues has been derived from the parabolic approximation of the band near the point  $k = 0$ . Due to the above mentioned properties of Schrödinger equation the eigenfunction  $\zeta_m$  does not depend on a constant shift of the potential.

Under this assumption it is possible to discretized the Schrödinger equation, by following the steps in the first chapter of [13], obtaining a matrix equation written as:

$$[H]\{\zeta\} = E[M]\{\zeta\} \quad (2.16)$$

where the sparse matrix  $[M]$  and  $[H]$  are the so called **Mass** and **Hamiltonian** matrix of the system. These are tridiagonal matrix with dimension equal to the square of the number of nodes, in which the space  $z$  has been discretized, they have to be define uniquely for each device and potential distribution.

It is important to notice that performing this discretization **Neumann** boundary conditions have been imposed at the two contacts of the device, by doing so the wave functions have null derivate at those point. This hypothesis is fair enough if a confined state is take into account, in fact it is expected that the probability of find an electron ( $|\psi|^2$ ) goes to zero outside the confined region. On the other hand, if a bulk resistor is taken into account, the Neumann boundary conditions lead to an unphysical estimation of charge at the

contacts. In a bulk semiconductor the solution is expected to have a form of a momentum eigenstate also in the  $z$  direction *i.e.* a complex exponential, but the wave-function found with the **Neumann** boundary condition has an *cosine-like* behaviour so what is missing to obtain a complex exponential behaviour is the *sine-like* part. The missing part can be obtained by solving the eigenvalue problem defined in eq.2.16 where the **Dirichlet** boundary conditions have been imposed at the two contacts. This new boundary condition forces the wave-function to be zero at the two edges of the device leading to a zero charge. Then if this two different solutions have booth computed and combined the overestimation of the carrier densities at the leads is mitigated.

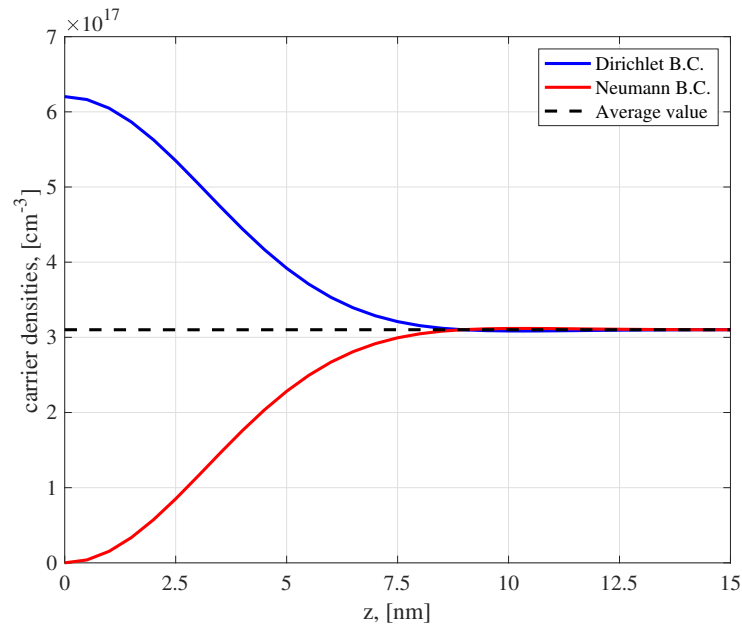


FIGURE 2.3: Comparison of carriers densities calculated by imposing the Dirichlet or Neumann boundary condition, with their associated average value, for a bulk resistor made of GaAs with a constant  $n$ -type doping equal to  $N_D = 10^{18} \text{cm}^{-3}$ . The incomplete ionization model has been introduced so the ionized doping charges are lower than the dopants densities, leading to a concentration of carriers lower than  $N_D$ .

In fig.(2.3) the electron concentration of a bulk resistor, calculated by imposing the Dirichlet and Neumann boundary conditions are depicted. At first glance, it is easy to see that far away from the boundary, in this particular case  $z \gg 0 \text{ nm}$ , the two carrier densities are equals and obviously coincident to their average. By moving closer to the contact the two densities start taking different values, and at the bulk's edge they behave in a totally different way. Here due to the Neumann boundary condition, the red curve is equal to zero while the blue one overestimates the carrier densities due to the absence of *sine-like* part. By performing the average value of the two different curves a constant result is obtained, meaning that the complex exponential behavior has been correctly included.

These considerations affect the calculation of charge only at the edges of

the structure in the study, so this correction is unnecessary for a long device where the population at the boundary is not important for the description of the device. Practically speaking, the final carrier densities  $n$  is the mathematical average of the ones found with the two dissimilar boundary conditions.

$$n(z) = \frac{n_D(z) + n_N(z)}{2} \quad (2.17)$$

When the results of simulations have been analyzed in the following chapters, the effects of boundary conditions have been no longer stress out, but it is very important for short device such as quantum wells. For all the geometry simulated with the Poisson-Schrödinger solver these two different boundary conditions have been introduced in the model, this new procedure doubles the simulation time due to the two different eigenvalue problems that have to be solved, but the simulation time remains acceptable if a one-dimensional structure is simulated.

Therefore, now it is possible to derive the electron density  $n(z)$  and  $p(z)$  knowing the conduction band  $E_C$  and the valence band  $E_V$  respectively, from those quantities the net charge density  $\rho$  can be written as:

$$\rho = q \cdot [p(z) - n(z) + N_D^+(z) - N_A^-(z)] \quad (2.18)$$

where  $N_D^+(z)$  and  $N_A^-(z)$  are the donor and acceptor ionized dopant density. Now, the derived charge density  $\rho$  has to be introduced in the Poisson equation, at thermodynamic equilibrium it can be written as:

$$\begin{cases} \frac{d}{dz} \left[ \epsilon(z) \frac{d\phi}{dz} \right] = -\rho(z) \\ \frac{d\phi}{dz} = 0 & z = 0; z = L \\ \rho(z) = 0 & z = 0; z = L \end{cases} \quad (2.19)$$

The device is terminated by ohmic contact at the edges ( $z = 0$  and  $z = L$ ) so the zero field condition has been imposed:

$$\mathcal{E}(z) = -\frac{d\phi}{dz} \Big|_{\text{contacts}} = 0 \quad (2.20)$$

Dirichlet boundary condition, shown in eq.(2.19), has been introduced in order to overcome the *ill-conditioning* of the problem, so the potential value has been fixed at the edges by imposing the neutrality condition, moreover it reaches this value with a zero derivate, according to the Neumann boundary condition [16].

Unfortunately,  $\rho$  depends on the potential too and so an iterative solution is needed, the **Newton method** has to be implemented.

MATLAB<sup>®</sup> as any other mathematical environment is not able to deal with differential equations so the eq. (2.19) has to be discretized, similarly to what has been done for the Schrödinger equation, with the aim to transform it into a matrix system that can be easily read in the computer framework. Calculation performed in **chapter 2** of [12] has been used for this implementation. The first step consists on the discretization of the domain  $z$ , where the ODE(2.19) is defined, into  $N$  nodes and  $N - 1$  elements, then the finite-box method has been applied and this equation has been transformed into a system of  $N$  equations, whose  $N$  unknown are the values of the unknown functions on the mesh nodes. The system (2.19) can be written, using the so called element-wise paradigm, as:

$$\epsilon_{i+\frac{1}{2}} \frac{\phi_{i+1} - \phi_i}{z_{i+1} - z_i} + \epsilon_{i-\frac{1}{2}} \frac{\phi_{i-1} - \phi_i}{z_{i-1} - z_i} + q[p_i - n_i + N_{D,i}^+ - N_{A,i}^-] = \quad (2.21)$$

$$F_i(\phi_{i-1}, \phi_i, \phi_{i+1}) = 0$$

In this formula is possible to easily distinguish two different parts, the first two terms includes **linearly** the unknown  $\phi$  while the latter depends in a non-linear way on the potential because the charge density is calculated from the Schrödinger equation that is anything but linear, this difference is crucial in the calculation of Jacobian matrix.

As explained in [12] (sect.2.3.3) Newton method is an iterative technique that update the results ( $\phi_i$ ) at each iteration  $k_{th} + 1$ , for every node, starting from the a potential at  $k_{th}$  iteration. Newton's method is introduced in order to calculate the variation of the potential between two consecutive iterations. This method is obtained by writing the first-order Taylor expansionist of the function that has to be minimized.

$$\frac{\partial F_i}{\partial \phi_{i-1}^{(k)}} \Delta \phi_{i-1}^{(k+1)} + \frac{\partial F_i}{\partial \phi_i^{(k)}} \Delta \phi_i^{(k+1)} + \frac{\partial F_i}{\partial \phi_{i+1}^{(k)}} \Delta \phi_{i+1}^{(k+1)} = -F_i(\phi_{i-1}^{(k)}, \phi_i^{(k)}, \phi_{i+1}^{(k)}) \quad (2.22)$$

The solution of this equation provides the update of the potential for each point of the discretized domain  $z$ . This equation can be now written in a matrix formalism as:

$$\mathbf{A}_{\phi\phi} \Delta \phi^{k+1} = \mathbf{r}_\phi \quad (2.23)$$

Therefore the derivate of eq.)2.21) has to be performed with respect to the potential in order to obtain the **Jacobian** matrix  $\mathbf{A}$ . As stated before  $F$  has a linear and non-linear part, for what concerns the first part the derivate is straightforward and it contains quantities independent on  $\phi$  and for sake of simplicity has not reported here, (the one used for the implementation in

code is the eq.(2.19) of [12]); On the other hand, the non-linear part has to be studied carefully.

The non-linear part is  $\mathbf{t}_\phi = q[p_i - n_i + N_{D,i}^+ - N_{A,i}^-]$ , so four different derivates have to be performed, (this number reduces to two if the full ionization is considered because in this case the dopant density is constant). First of all, the derivate of eq.(2.12) has performed following the assumption made in [15], where it is stated that the wave-functions  $\zeta_m$  and the energies of the bound states  $E_m$  with respect to the bottom of the well do not change for a small change in potential  $\phi$ . So it can be assumed that:

$$\frac{\partial |\zeta_i^{(k)}|^2}{\partial \phi_i} = 0 \quad \text{and} \quad \partial(E_m - E_F) = -q\partial\phi_i \quad (2.24)$$

and equation 2.12 become:

$$\frac{\partial n(z_i)}{\partial \phi_i} \simeq \frac{q}{k_B T} \frac{1}{\pi} \sum_{m=1}^{N_k} \sum_{m=1}^{N_{eig}} |\zeta_m(k, z_i)|^2 \cdot \frac{\exp\left(\frac{E - E_f}{k_B T}\right)}{\left(1 + \exp\left(\frac{E - E_f}{k_B T}\right)\right)^2} k_n \Delta k_n \quad (2.25)$$

For what concerns the holes, starting from eq.(2.13), with the same approximation, it is possible to obtain a formula very similar to the one depicted for electrons. Finally, if the incomplete ionization is considered the derivate of ionized dopant density w.r.t. the potential  $\phi$  has to be introduced into the  $\partial\rho/\partial\phi$ , the model described in **appendix B** of [16] has been used for this implementation.

### 2.1.3 Density of states

The solution of the Schrödinger equation provides a lot of information for the system in studying, one of them is the **integrated density of state (IDOS)**, *i.e.* a function that measures how many electron energy levels can be found below a given energy per unit volume of a solid. By following this definition the derivation of this quantity is straightforward.

It has already been seen that the Schrödinger equation gives as results a set of eigenvalues  $E_m$ , these quantities provide the allowed set of energy of the quantum states. Now if these eigenvalues are introduced in a sort of counting problem and integrated within a certain energy it is possible to obtain a dimensionless number that counts the available states for the electrons independently of the position, it is important to recall that the Schrödinger equation does not consider the **spin** so this result has to be multiplied by 2,

in formula the IDOS reads:

$$\text{IDOS}(E) = 2 \cdot \sum_{i=0}^{E_i < E} \int_0^L |\psi_i(z)|^2 dz \quad (2.26)$$

In a classical framework, these eigenvalues are able to vary continuously leading to a smooth IDOS on the other hand in quantum mechanics, especially on confined sub-regions, these values are separated in energy and so the IDOS behaves as a step-wise function.

## 2.2 Landscape Potential

### 2.2.1 The need of an effective potential

In the last decade's carrier transport in semiconductor systems has been mostly described by the classical drift-diffusion(DD). Unfortunately, this model does not take into account the quantum effects: tunneling and quantum confinement, so it is not able to describe devices that work on those effects, such as modern detectors or LEDs. In other words, the classical DD describes the carriers as if the whole device is a bulk resistor and so by neglecting the tunnelling effects the potential seen by the electrons is different from the real one.

An earlier solution to this problem is to replace the superlattice with a fictitious device characterized by a band gap calculated in an effective way, in such a way that the superlattice is described by a bulk resistor with a constant energy gap  $E_G$ , in such a way that the barriers, that limit the flow of carriers in the device, are not present in the calculation of drift-diffusion model. This was one of the first methods that try to provide a link between the classical models, developed for the flow of carriers in a bulk resistor, and the quantum confinement due to heterostructure or doping. The main limitation of this approach is that the physical effects inside the device were not considered in a direct way, this could lead to quite unphysical behavior and hence this is a tool that must be handled with care.

The main idea of replacing the real potential with a new one that can be handled by a classical drift-diffusion model had other implementations, the difference among them is how this new potential is defined. A new definition of this potential is done by modeling the physical effects inside the confinement regions obtaining a position-dependent effective potential  $\phi(r)$ . For example, if a multiple quantum well is taken into the study, the system is characterized by a certain number of barriers and wells, if in a specific region the carriers can tunnel through the original barrier, due to the spatial tail that crosses the potential barrier, the effective potential will be lower than the classical one reducing the barrier seen by the carriers. Now at least in theory, if this new effective potential is introduced in a drift-diffusion model, it will be able to describe the tunneling current in a classical way. Unfortunately, there is not yet a model that describe quantum current originates from scattering events or phonon-assisted hopping between quantum state is still considered in an effective way by the mobility  $(\mu_n, \mu_p)$  [8].

In 1952 Bohn proposed to calculate this kind of potential from the solution of the Schrödinger equation. But, as it is well known, the Schrödinger equation is an eigenvalue problem and its numerical evaluation is high time consuming especially for a big device with quite a high number of mesh points or multidimensional system [17].

Therefore to achieve a fast numerical implementation the Schrödinger equation does not have to be solved. A possible model, that overcome this calculation, is the **Landscape potential model** proposed by Filoche and Maybora in 2012. [7] The main advantage of this new effective potential is the tremendous time saving when multidimensional systems are taken into the analysis, furthermore, even in a 1D simulation, it allows to study long devices even with a fine mesh and still having an acceptable simulation time. So how this potential is defined and why does it look so promising for the modelling superlattice or resonant tunnelling diode (RTD)?

## 2.2.2 Landscape Potential

In this section has been described the main aspects of the Localization Landscape theory presented for the first time in [7]. Filoche introduced this potential with the aim to solve a well-known problem, the localization due to **Anderson disorder**, without care too much about the physical mechanism that gives rise to it. Practically speaking, his aim is to find a model that, given a geometry and its potential distribution, predicts in which subregions one can expect localized standing waves to appear, and at which energy.

In addition, it is well known that a localized state is a standing wave that is maintained in a small sub-space of domain  $\Omega$ , usually this wave and its vibrational energy  $E$  can be rigorous derived by solving the ordinary Schrödinger equation with Dirichlet boundary condition define of the contour of domain  $\partial\Omega$ .

$$\hat{H}\psi = -\frac{\hbar^2}{2m_{eff}}\Delta\psi + V\psi = E\psi \quad (2.27)$$

where:

$$u|_{\partial\Omega} = 0 \quad (2.28)$$

This equation is an eigenvalue problem that can be solved numerically performing a discretization of the domain, as it has been shown in sec.(2.1), this procedure becomes computationally infeasible for high numbers of mesh point or more than one-dimensional device. It is also easy to notice, that from the shape of potential  $V$  it is impossible to extract any kind of information about the profile of quantum state or even less on areas of confinement.

The remarkable intuition of *Filoche et. al.* is to do not solve anymore an eigenvalue problem, but to replace the right-hand side of eq.(2.27) with an

unitary quantities, obtaining the equation:

$$\hat{H}u = -\frac{\hbar^2}{2m_{eff}}\Delta u + Vu = 1 \quad (2.29)$$

where:

$$u|_{\partial\Omega} = 0 \quad (2.30)$$

By performing this substitution the eq.(2.29) is not anymore an eigenvalue problem and so it can be resolved easily and with low computational time even for large systems.

It is important to spend some word about the sign of Hamiltonian operator and on the sign of solution  $u$ :  $\hat{H}$  is an elliptical second-order operator, which is positive only if  $V(x)$  is positive everywhere and in this case the solution  $u$  will be positive as well. If these conditions are met  $u$ , as it is described in [7], is the sought landscape potential and it is demonstrated that the subregions hosting localized eigenfunctions are delimited by the valley lines of the graph of  $u$ .

The main reason of this behaviour can be understood if the following inequality, that it is satisfied by any normalized eigenfunction  $\psi$  of  $\hat{H}$  with eigenvalue  $E$ , is taken into account: (for mathematical proof: APPENDIX)

$$|\psi(r)| \leq Eu(r)$$

where  $E$  is the mode energy and  $\psi$  is the mode amplitude normalized. Therefore, this inequality forces the modules of  $\psi$  to be small where the potential  $u$  has a minimum, this locus of points is called **valleys**. According to the dimensionality of domain, these valleys can be surface, lines, or single points if a 3- 2 or 1-dimensional device is investigated, respectively. So with this potential is possible to define subregions, that are a partition of the whole domain, wherein each of these subregions the carriers are localized and the strength of this localization can be extrapolated from the peaks of function  $u$ . The reason of this "fancy" name, localization landscape potential, can be better understand if an other function is introduced [8]

$$W(\vec{r}) = 1/u(\vec{r})$$

first off all, it is importance to notice that the physical dimension is equal to an energy, since  $u$  is a solution of eq. (2.29),  $W$  is indeed homogeneous to an energy and so it can be consider as an **effective confining potential**. Therefore,  $W$  is essentially the inverse of  $u$ , in this case, the peaks determine the confinement of quantum state inside a certain region, following the analogy explained above, these peaks can be seen as *watersheds* that confined water in

a jagged montane landscape.

By reformulating this concept in a more formal way it is possible to say that the localization subregions at energy  $E$  can be calculated by filling the effective potential  $W$  up to the height  $E$ , and then observing the extent of flooded basins. Within this new framework, the exponential decay length of the Anderson can be derived but it is out the purpose of this thesis.

In summary, the quantum confinement due to the inferential pattern of waves in the potential  $V$  can be described in a classical way adopting the new effective potential  $W$ .

This potential will be implemented into a **semi-classical Poisson and drift-diffusion** model and compared to already existing models that take into account the wave nature of electrons. At equilibrium the explained Poisson-Schrödinger solver is used as a term of comparison while out of equilibrium a model that includes quantum effect such as the tunneling current is needed: the non-equilibrium Green's function formalism (NEGF) has been selected. A better description of how this model has been implemented is given in the following sections.

### 2.2.3 Eigenvalue estimates

It has been shown that effective potential  $W$  properly describe the confinement of carriers due to an external potential or molecular disorder, but it can be proved [8] that this new developed mathematical tool can be used to give an estimation of the effective value of quantum energy ground-state. By decomposing eq.(2.29) on the basis formed by the eigenfunction  $\psi_i$  of the Hamiltonian is possible to prove that in each localization subregion labelled as  $\sigma_m$  and  $\psi_0^{(m)}$  the associated ground state can be derived with the equation:

$$u \simeq \frac{\langle 1 | \psi_0^{(m)} \rangle}{E_0^j} \psi_0^{(m)} \quad (2.31)$$

From eq.(2.31) is possible to write that  $\psi_0^{(m)}$  is almost proportional to the localised function  $u$  in that subspace, then with a few steps and introducing  $W \equiv u^{-1}$  is possible to write for a 1D device:

$$E_0^{(m)} = \frac{\int_{\sigma_m} u(z) dz}{\int_{\sigma_m} |u(z)|^2 dz} \quad (2.32)$$

Therefore it is possible to directly estimate the value of fundamental energy by knowing the shape of localization landscape potential  $u(z)$ .

### 2.2.4 Density of states and carrier densities

In conclusion, it is essential to understand how this new landscape potential can be used to calculate the carrier densities. To do so, some consideration on the local density of state (LDOS) has to be performed.

The density of states gives the number of allowed electrons (or holes) states per volume at a given energy, if a non infinite bulk device is taken into analysis no confinement occurs and the classical local density of state can be easily derived by expressing the available states per unit energy in the  $k$ -space obtaining:

$$\text{LDOS}(E, \vec{r}) = \frac{1}{2\pi^2} \left( \frac{2m_e^*}{\hbar^2} \right)^{\frac{3}{2}} \sqrt{E - E_C(\vec{r})} \quad (2.33)$$

By definition, it is possible to find the electrons(holes) density by integrating the number of allowed states per volume (LDOS) multiplied by its probability of occupation at a given energy described by the Fermi function:

$$n(\vec{r}) = \int_{E_C(\vec{r})}^{+\infty} \frac{1}{1 + \exp\left(\frac{E - E_F}{k_B T}\right)} \text{LDOS}(E, \vec{r}) dE \quad (2.34)$$

If the local density of state is equal to eq.(2.33) this integral can not be solved analytically, the eq.(2.34) can be re-written introducing the Fermi integral of order 0.5 ( $\mathcal{F}_{\frac{1}{2}}$ ).

$$n(\vec{r}) = N_C \mathcal{F}_{\frac{1}{2}} \left( \frac{E_F - E_C}{k_B T} \right) \quad \text{where} \quad N_C = 2 \left( \frac{m_e^* k_B T}{2\pi \hbar^2} \right)^{\frac{3}{2}} \quad (2.35)$$

The model described above is a classical description that allows predicting the carrier densities inside a semiconductor without taking into account the quantum effects that can arise due to confinement.

It has been shown that in the landscape potential all these effects are considered effectively by introducing a new potential and the carriers under this potential behave as classical particles. By following the hypothesis made in [8] it is possible to replacing the original potential ( $E_C$ ) with  $W_C$  in eq.(2.33) to accurately estimate the local density of state of a confined system by.

$$\text{LDOS}(E, \vec{r}) = \frac{1}{2\pi^2} \left( \frac{2m_e^*}{\hbar^2} \right)^{\frac{3}{2}} \sqrt{E - W_C(\vec{r})} \quad (2.36)$$

The physical meaning of this expression is, for a given device, the local density of state is equal to the one of an infinite medium with identical material composition and a parabolic band whose minima energy would be  $W(\vec{r})$ .

Moving to a 3D system where a confining potential is present along the  $z$  direction there is a translational invariance in the two other directions  $x, y$ , so it is possible to show that quantum states are products of 1D and 2D states. The total density of states can be found by convolving the 1D and 2D LDOS [8], the derivation of these last formula is very similar to the 3D LDOS and for sake of simplicity will not be reported here:

$$\begin{aligned} \text{LDOS}_{3\text{D}}(E, z) &= \frac{1}{4\pi^2} \left( \frac{2m_e^*}{\hbar^2} \right)^{\frac{3}{2}} \int_{W_C}^E \frac{dE_1}{\sqrt{E_1 - W_C(z)}} \\ &= \frac{1}{2\pi^2} \left( \frac{2m_e^*}{\hbar^2} \right)^{\frac{3}{2}} \sqrt{E - W_C(z)} \end{aligned} \quad (2.37)$$

It is straightforward to see that the above expression is identical to the one found for the bulk device so the carriers can be calculate by the formula shows in eq.(2.34) where the potential  $E_C$  has been replaced by  $W_C$ .

$$n(\vec{r}) = N_C \mathcal{F}_{\frac{1}{2}} \left( \frac{E_F - W_C}{k_B T} \right) \quad (2.38)$$

This is one of the most important steps in the delineation of the Localize Landscape model, by calculating the carries in this way leads to a tremendous reduction of simulation time w.r.t a Schrödinger equation and furthermore the system in the study can be considered as a classical one. By doing so, all the already existing models for classical simulation can be used, just by replacing the previous classical potential with the localization landscape potential. In the following section, it has been explained how this potential can be introduced inside a Poisson drift-diffusion iterative model to simulate a quantum structure out of equilibrium.

### Integrated Density of State

To provide a coherent comparison between the Landscape model and the already explained Schrödinger-Poisson solver, also in this case the integrated density of State (IDOS) has to be defined. By considering the uncertain principle, for a 1-dimensional geometry,  $\Delta z \Delta k \simeq 2\pi$  the one-particle quantum state spreads in phase space with a volume equal to  $2\pi$ , following [8], is possible to show that the number of energy states below given energy, that is the wanted IDOS, has an asymptotic behavior so-called Weyl's law. This law states that the asymptotic behaviour of IDOS is equivalent to  $\mathcal{V}(E)/(2\pi)$

where  $\mathcal{V}$  is the volume in the phase space determine by  $\hat{H} < E$ . Tacking in mind the above considerations mede for this new potential  $W_C$  is possible to write Hamiltonian as:

$$H(z, \vec{k}) = \frac{\hbar^2 k^2}{2m_e^*} + W_C(z) \quad (2.39)$$

then introducing the spin factor, IDOS can be calculated from:

$$\begin{aligned} \text{IDOS}(E) &= \frac{2}{2\pi} \int_z \int_{H < E} dk dz \\ &= \frac{2}{\pi} \int_z \sqrt{\frac{2m_e^*(E - W_C(z))}{\hbar^2}} dz \end{aligned} \quad (2.40)$$

Before going on, it is important notice that the classical formulation of IDOS can be obtained simply replacing the landscape potential by the conduction band edge, furthermore if the holes are considered instead of the electron the developed localization landscape model still works properly, if the necessary substitution of terms are performed.

### 2.2.5 Potential reference

A crucial proprieties of Landscape potential that have to be underlined before proceeding in further calculations and analysis is the effect that an off-set has on the final calculated effective potential  $W$ . Considering the Schrödinger equation (2.27), if an offset is introduced inside the potential  $V(\vec{r})$  the only visible effect on the energy eigenvalue is that has been shifted by the same offset introduced (this propriety has already used to deal with the transversal energy component)

On the other hand, If a constant value  $K$  is introduced in the eq.(2.29) becomes:

$$-\frac{\hbar^2}{2m_{eff}} \Delta u_K + (V + K)u_K = 1 \quad (2.41)$$

leading to a potential  $W_K = u_K^{-1}$  very close to  $K$ , furthermore if the inequality

$$|\psi| \leq (E + K)u_K$$

is considered the product  $K \cdot u_K$  become close to 1 and this inequality is almost always satisfy, and therefore  $u_K$  is not anymore able to describe the localization of states in certain subregion of the domain. The reference of potential  $V(z)$  should be chosen as the smallest possible but in such a way that

the Hamiltonian remains a positive operator.

In this thesis, both the conduction and the valence have been minimized before proceeding to the calculation of  $W_C(W_V)$  and then the subtracted offset is readded later to  $W_C$ .

## 2.3 Out-of-equilibrium

The considerations and models described above hold only at equilibrium, where no external field has been applied. From a practical point of view, those analyses will not be very useful if real working devices, like lasers or a photodetector, are taken into study.

Classically, a bulk resistor out of equilibrium can be studied by resolving the well known Poisson equation coupled with drift-diffusion, this model is commonly used to describe the transport and optical properties, by treating the carriers as semi-classical particles with a renormalized effective mass. However, it is also possible to introduce implicitly many results of **quantum theory** as energy levels, the density of states, quantum Fermi-Dirac statistics, and **transport parameters**, such as carrier mobilities and diffusion coefficients.

The optical proprieties usually is taken into account by means of the *ABC* model for total recombination rate in semiconductor photonic devices. This is an empirical model that consider the non-radiative recombination (*e.g.* thermal in the lifetime approximation) and the Auger nonradiative recombination (proportional in quasi-neutrality to the cube of carrier concentration) and express the total recombination rate as:

$$R_{tot} = A \cdot n + B \cdot n^2 + C \cdot n^3 \quad (2.42)$$

The coefficients *A B* and *C* describe the *Thermal*, *Radiative* and *Auger* respectively. These parameters has been considered in the following as given parameters and non-further consideration has been done on this model.

Moreover, the coupled Poisson and Drift-Diffusion equations system, if no further changes are made, is not able to consider the quantum transport of carriers inside the device, for example, if a resonant tunnel diode is simulated the current found with this technique will be very small due to the presence of barriers that block the flowing of electrons and holes, this can be explained considering the inability of the model to consider tunneling effects caused by the spatial tails of the eigenstates that cross the potential barriers.

In literature, the non-equilibrium Green's function formalism (**NEGF**) has been introduced to overcome this problem, in fact, it provides a proper description of the quantum effect, as for example the tunneling current. Unfortunately, this model is practically unusable for high-dimensionally or long device due to its extremely high computational time. In this study NEGF out

of equilibrium has been implemented for a 1D structure by means of Büttiker's probes, (an exhaustive description of implementation is given later) in order to have a term of comparison for the new Landscape model out of equilibrium proposed in [17].

The main idea proposed by Filoche is to introduce the well-described Landscape potential into a semi-classical Poisson drift-diffusion solver, in such a way that all the quantum effects are encoded inside this effective potential. If this hypothesis is valid it is possible to consider whatever device as a classical bulk one where all the non-classical effects are taken into account by this new potential.

### 2.3.1 Description of the model

In the following after a brief recap of the classical drift-diffusion model and its solution technique, it is explained how the Landscape potential  $W_{LL}$  has been introduced in this system of equations.

Focussing on a stationary 1-dimensional problem, it is possible to show that the Poisson Drift-Diffusion problem (from now on labelled as PDD), reads:

$$\begin{cases} \frac{\partial}{\partial z} \left( \epsilon \frac{\partial \phi}{\partial z} \right) + q(p - n + N_D^+ - N_A^-) = 0 \\ -\frac{1}{q} \frac{\partial J_n}{\partial z} + U_n = 0 \\ +\frac{1}{q} \frac{\partial J_p}{\partial z} + U_p = 0 \end{cases} \quad (2.43)$$

where the drift-diffusion constitutive relation derived from the Boltzmann transport equation are:

$$\begin{cases} J_n = -qn\mu_n \frac{\partial \phi}{\partial z} + qD_n \frac{\partial n}{\partial z} \\ J_p = -qp\mu_p \frac{\partial \phi}{\partial z} - qD_p \frac{\partial p}{\partial z} \end{cases} \quad (2.44)$$

$U_n$  and  $U_p$  are the recombination rate for the electron and holes, their full description is without the purpose of this thesis.

By introducing eq.(2.44) into eq.(2.43) is possible to see that this problem is a system of partial differential equations, namely Poisson's electron continuity and hole continuity, with three unknowns:

- **the electrostatic potential  $\phi$** : solution of the Poisson equation.
- **the electron density  $n$** , from which is possible to calculate the current density  $J_n$ .

- **the hole density**  $p$ , equivalently to electron density determines the hole current density  $J_p$ .

Similarly as before, this problem will be treated by a generalized Newton's method leading to a matrix equation:

$$\begin{bmatrix} \bar{\bar{A}}_{\phi\phi} & \bar{\bar{A}}_{\phi n} & \bar{\bar{A}}_{\phi p} \\ \bar{\bar{A}}_{n\phi} & \bar{\bar{A}}_{nn} & \bar{\bar{A}}_{np} \\ \bar{\bar{A}}_{p\phi} & \bar{\bar{A}}_{pn} & \bar{\bar{A}}_{pp} \end{bmatrix} \cdot \begin{bmatrix} \Delta\bar{\phi} \\ \Delta\bar{n} \\ \Delta\bar{p} \end{bmatrix} = \begin{bmatrix} \mathbf{r}_\phi \\ \mathbf{r}_n \\ \mathbf{r}_p \end{bmatrix} \quad (2.45)$$

This matrix problem has been written by following the notation described in [12], where each sub-matrix  $\bar{\bar{A}}$  has two different sub-scripts: the first one is related to the equation to be assembled while the second indicates the unknown considered. For example the matrix  $\bar{\bar{A}}_{\phi n}$  contains the coefficients of derivate of the Poisson equation w.r.t. the electron density. For sake of notation, both the electron density and electron continuity equation are labeled with the same letter.

The vector quantity  $\Delta u$  embodies the incremental of the unknown quantities at the subsequent iteration, until convergence is achieved, while vector  $\mathbf{r}$  is the residual of the minimization problem defined in eq.(2.43).

The definition of these matrix terms is out of the purpose of this master thesis, the results obtained in [12] has been used for the implementation, and for sake of simplicity, it will not be reported here.

The main advantage of this method is the speed, it can be seen that for a one-dimensional device, it reaches the convergence within few steps if a good initial guess is provided, usually if the bias is not so high is enough to choose equilibrium's condition to assemble  $u_0$ .

Whit the aim to use this method to describe **quantum devices** the landscape potential has to be introduced, but how can it be done?

### 2.3.2 Moving to Landscape potential

At equilibrium, the landscape potential has been introduced inside the Poisson solver just by replacing the classical potential  $E_C(E_V)$ , in the carrier densities calculation, with the new  $W_C(W_V)$ . However, in this new iterative problem, the carriers can not be calculated by the eq.(2.38) because electron and hole densities are both unknowns of the system, so a different *modus operandi* has to be used.

The coupling between Poisson and drift-diffusion described in the previous section was the more general approach possible, where just a discretization along the dimension  $z$  has been introduced, but for an effective stable numerical implementation further correction and considerations have to be done. First of all, for this numerical implementation the Fermi statistic has been used instead of the Boltzmann one, and on the second-hand devices in the

study all are made up by heterostructure and a correction on the definition of the potential has to be introduced, finally the Scharfetter-Gummel discretization scheme is needed to achieve a stable solution of the iterative Newton-method.

Above all, it can be interesting and illustrative to spend some words on the Scharfetter-Gummel discretization, a method that has been proposed in order to overcome the numerical instability (in particular for device discretized with not so high numbers of mesh point or a strong electric field) of the general method described in the previous section. The need for this new discretization method can be better understood if the dependence of electrons concentration on the potential  $\phi$  is taken into account: by using the Boltzmann approximation is straightforward to see that the electrons concentration depends exponentially on the potential, so using the same *discretization step* for both two quantities do not look like a clever approach. Furthermore, it has been shown, from fluid dynamic studies, that when two physical phenomena are competitive in a convective flow eq.(2.44) drift and diffusion standard numerical approach are unstable.

The purpose of Scharfetter-Gummel discretization model is to provide a stable discretization of the drift-diffusion constitutive relations and so be able to determine the current density between two nodes, the unknown will not be anymore the carrier densities  $n$  and  $p$  but the current density  $J_n$  and  $J_p$  where a linear variation between two nodes is still a fair discretization. The formula for **continuity equations** within this new frameworks reads:

$$\begin{cases} J_{n,ij} = q \frac{D_n}{l_i} \left[ n_j \mathcal{B} \left( \frac{\phi_j - \phi_i}{V_T} \right) - n_i \mathcal{B} \left( \frac{\phi_i - \phi_j}{V_T} \right) \right] \\ J_{p,ij} = q \frac{D_p}{l_i} \left[ p_i \mathcal{B} \left( \frac{\phi_j - \phi_i}{V_T} \right) - p_j \mathcal{B} \left( \frac{\phi_i - \phi_j}{V_T} \right) \right] \end{cases} \quad (2.46)$$

where  $\mathcal{B}(x)$ , the *Bernoulli function*, is define as:

$$\mathcal{B}(x) = \frac{x}{\exp(x) - 1} \quad (2.47)$$

The unknowns  $J_n$  and  $J_p$  do not have an exponential dependence on the other unknown of the problem the potential  $\phi$ , moreover, it has to notice that within this new formalism it is not possible to distinguish the *drift* and *diffusion* contribute to the total current density.

These method was derived by considering an homogeneous material and **Boltzmann** statistic. Now if the Fermi statistic and heterostructure is introduced in the model it is still possible to show that the continuity equation for electrons and holes current can be expressed with eq.(2.44), where the potential has been modified by a new correction terms. The new potential is:

$$\phi_{eq}^{(n)} = \phi + \left[ \frac{\chi}{q} + \frac{k_B T}{q} \ln(N_C) + \frac{k_B T}{q} \ln(\gamma_n) \right] \quad (2.48)$$

the correction terms are those inside the square brackets, the first two terms are coming from the introduction of heterostructure, while the last one is due to the consideration of Fermi statistic, the factor  $\gamma_n$  is simply the ratio between population of electron calculated with **Fermi** statistic divided by the one found with **Boltzmann**. The eq.(2.46) coupled with the potential defined in eq.(2.48) has been used to built-up the matrix for the Newton iteration technique. It has to be reminded that the method discussed so far is still the classical one, it does not yet take into account the quantum effects. With the aim to include them the Landscape potential has to be somehow introduced. Before going on, it is relevant to discuss the so-called diffusion coefficient  $D_n, p$  introduced in eq.(2.46) defined as:

$$D_n = \mu_n k_B T$$

The mobility  $\mu$  define with Einstein relation is a **bulk mobility**, that do not obviously consider tunneling effects, so the transport of carriers is described classically, even in the following when landscape potential is introduced. The mobility is still considered as a bulk one and all the quantum effects are encoded only in the potential. Hence tunneling current will be described by the lowering of the effective potential, instead, there is no model yet able to describe with a full quantum model for the quantum-current originated from the phonon-assisted hopping between different eigenstates and this effect has to be described through effective mobility, the effects of this latter contribution to the current will not be discussed.

It has already been discussed that the landscape potential works properly only if its offset has been minimized and the relative Hamiltonian is positive, out of equilibrium the classical potential seen by the carriers is difficult to minimize due to the external electric field that bends the band diagram. It can be decomposed into two contributes: the one due to the heterostructure, usually with a higher frequency variation, and the one due to the external electrical field with a larger and smother variation. A possible solution to overcome this problem, which has also the positive effect of speed up the simulation, is to apply the localization landscape theory only on the component of potential independently on the externally applied bias, and regain the total one just by summing the two contributes.

In others words the electrostatic potential  $\phi$  of the Poisson equation and the uncorrected one of eq.(2.48) will not be directly influenced by the LL potential but all the quantities derived from it (conduction and valence band, correct potential..) will be reshaped with the potential  $\Delta E_C^{LL}$  found at equilibrium. So this model can be seen as if a classical Poisson drift-diffusion has been applied to a device where the conduction and valence band are described by

this new smoother version of potential obtained from Landscape theory. As an example, the factor  $\gamma_n$  is defined as :

$$\gamma_n = \frac{n}{n_b}$$

here both the electron density calculate with Fermi and the one with Boltzmann needed a conduction band edge and it will obtained with:

$$E_C = \phi + \Delta E_C^{LL}$$

Where  $\Delta E_C^{LL}$  is the effective correction of the potential at equilibrium, where all the confinement effects are encoded. It straightforward to notice that also the first two factors inside the square bracket in eq.(2.48), that are constant and depend only on geometry, has been reshaped by the Landscape potential. For the valence band and the hole concentration, all the considerations and the corrections terms introduces so far are still valid with the proper substitutions.

## 2.4 NEGF and Buttiker probes

Finally, the NEGF approach has been considered. This method has been used for both equilibrium and out-of-equilibrium simulation with the aim to provide a further term of comparison for the results obtained with the landscape potential. Non-equilibrium Green's function (NEGF) method is one of the most popular employed models to describe carrier dynamics in open quantum systems. In literature, this approach has been applied to a considerable collection of devices leading to a successful prediction of carriers transport and optical properties. However, all these promising studies are characterized by the same problem: the NEGF approach is very high time-consuming and its mathematical formalisms can be tricky and complex.

In this section, a brief explanation of the used NEGF method is presented underlining the approximation performed made to reduce the complexity of equations and to achieve a reasonable simulation time. Furthermore, it is important to recall that this method has been introduced in this thesis just to perform a comparison, and it has been applied to already existing results, so depending on the methodology used for the analysis NEGF should be able to adapt its parameters or inner approximation in such a way that there is a perfect match in the frameworks of two different study. All these considerations will be better explained in chapter 3 where the simulations results are shown.

Usually, in NEGF calculation all the scattering processes are set to zero, and the system is described as a ballistic device. This first approximation is fair enough if very short devices with high mobility and low temperature are taken in the study but unfortunately, this is not the case. Therefore, scattering events have to be introduced into the model. The Büttiker probes approach, in which the individual physical scattering event is replaced by global energy and momentum self-energy described by a scattering Fermi level [21], seems to be a reasonable choice. For a complete description of the NEGF approach one usually has to achieve an iterative solution with the Poisson equation, similarly to what has been done in sec. 2.1 for the Landscape model, an expert reader can quickly understand that a self-consistent solution requires a definition of boundary conditions and the insertion of coupling with the contacts, increasing the complexity of implementation and the simulation time. Moreover the obtained results, as for example the conduction band, coming from this iterative solution can not be mutually consistent with the one found with the Landscape potential, leading to an inconsistent comparison. For the following simulations, the input potential and Fermi level of the contacts reservoir are those found with the iterative LL-PDD or Poisson Schrödinger simulation. The only iterative procedure presents in the NEGF implementation is the inner-loop implemented for the conservation of current inside the Büttiker probes.

### 2.4.1 NEGF

Firstly, the NEGF formalism has to be defined, for a geometry discretized along the heterostructure's growth direction  $z$ . It has already been underlined in eq.(2.2) that the wave-function of a quantum states can be decomposed into a product of plane wave and a shape function that slowing varying along the direction of confinement. Here, only the latter contribute has been used for the derivation of NEGF matrix formalism. By using the approach described in [13] is possible to write down a set of uncoupled equations that allows to derive physical observable, such as the carriers and current densities, these matrix can be written as:

$$G^R(\vec{k}, E) = [EM - H(\vec{k}) - \Sigma^R(\vec{k}, E)]^{-1} \quad (2.49a)$$

$$G^A(\vec{k}, E) = (G^R(\vec{k}, E))^\dagger \quad (2.49b)$$

$$G^\lessgtr(\vec{k}, E) = G^R \Sigma^\lessgtr G^A \quad (2.49c)$$

Where  $G^R$  is the retarded green function,  $G^\lessgtr$  the lesser and grater green functions, and finally  $\Sigma^\lessgtr$  is the greater and lesser self energy that can be derived from:

$$\Sigma^< = i[f_{FD}(E(\vec{k}) - \mu)\Gamma(\vec{k}, E)] \quad (2.50a)$$

$$\Sigma^> = i[f_{FD}(E(\vec{k}) - \mu) - 1]\Gamma(\vec{k}, E) \quad (2.50b)$$

where the broadening factor  $\Gamma$  is:

$$\Gamma(\vec{k}, E) = i[\Sigma^R(\vec{k}, E) - \Sigma^A(\vec{k}, E)] \quad (2.51)$$

in this latter formula the retarded and advanced self energy [ $G^A := (G^R)^\dagger$ ] have been introduced. It is easily detectable that both the Green's and Self energy matrices depend on the energy and on the wave-vector ( $\mathbf{k}$ ).

It important to underline that the Hamiltonian  $\hat{H}$  of the system does not depend on transversal energy level ( $E$ ), while in the retarder self energy  $\Sigma^R$  are encoded the information of the coupling with the left and right reservoir and the self energy of the Büttiker probes. All Green's functions and self-energies are matrices derived from the discretization in space over the direction  $z$ , furthermore in the MATLAB implementation they have been built up as **sparse** matrix to further reduce the computation cost.

It is possible to show that, from the retarded Green function all the physical quantities like carrier densities or current density can be derived, here is reported the used formula to calculate the electron spectral density and the

current spectral density for a 1-dimensional device:

$$n(z_i, E) = -2 \frac{\Delta k}{2\pi} i \sum_{k_j} k_j G_{i,i}^<(k_j, E) \quad (2.52a)$$

$$J(z_i, E) = 2 \frac{q}{\hbar} \frac{\Delta k}{2\pi} \sum_{k_j} [(H_{i+1,i}(k_j) - EM_{i+1,i}) G_{(i+1,i)}^<(k_j, E) - G_{(i,i+1)}^<(k_j, E) (H_{i+1,i}(k_j) - EM_{i,i+1})] \quad (2.52b)$$

In these formulas the dependence on transversal vector  $\vec{k}$  is still consider directly, as it will better discuss later, this approach has only been used at equilibrium for short device simulation. The reason under this choice is that, as soon as the complexity of the structure increases, perform a sum on the discretized domain  $k$  becomes computation unsustainable. So for long devices simulation and for the ones out of equilibrium, where the inner loop on Büttiker Fermi level is introduced, the integration over the  $k$  vector will be perform analytically.

## 2.4.2 Scattering

In a ballistic simulation a device is connected at left and right edges at two reservoirs characterized by their Fermi levels  $(\mu_L, \mu_R)$ , respectively. They are able to exchange with the system momentums and carriers, these two regions labeled as Source and Drain injects carriers from a side and recollect them from the other side. The number of injected and extracted electrons is the same so the current is conserved. By studying the behavior of these injected carriers is possible to fill the density matrix and so derive all the needed physical quantities.

The Büttiker probes are introduced in order to model the **dissipative transport** phenomenologically within the device, these probes perturb the Hamiltonian similarly to what the source and drain reservoirs do. These probes can be seen as multiple internal reservoirs coupled with the device, the main difference with respect to the D. and S. is that this new set of reservoirs can not exchange particles within the system but only change the momentum of the electrons in order to bring the system in equilibrium (a ballistic device is as far from equilibrium as it can be).

This process can be seen as if a Büttiker probe extracts electrons from the device, perturbs those electrons energy and momentum, and then reinjects them in the device with a different momentum distribution without changing their number. The associated Fermi level of Drain and Source describes how they exchange carriers with the device, following this result is possible to demonstrate that even the Büttiker probes have their own Fermi levels

( $\mu_{BP}$ ), that describes, similarly to  $\mu_R$  and  $\mu_L$ , how those fictitious reservoirs extract and inject electrons into the system. However, it should be notice that the introduction of scattering events inside the simulation framework does not have to break the conservation of current. Therefore, those Fermi level have to be selected in such a way that carriers are conserved at each probe center leading to a zero probes current, this implies that the total current density is constant in space. A primal schematic representation of how those Fermi levels is updated in order to achieve such condition is given in fig.(2.4).

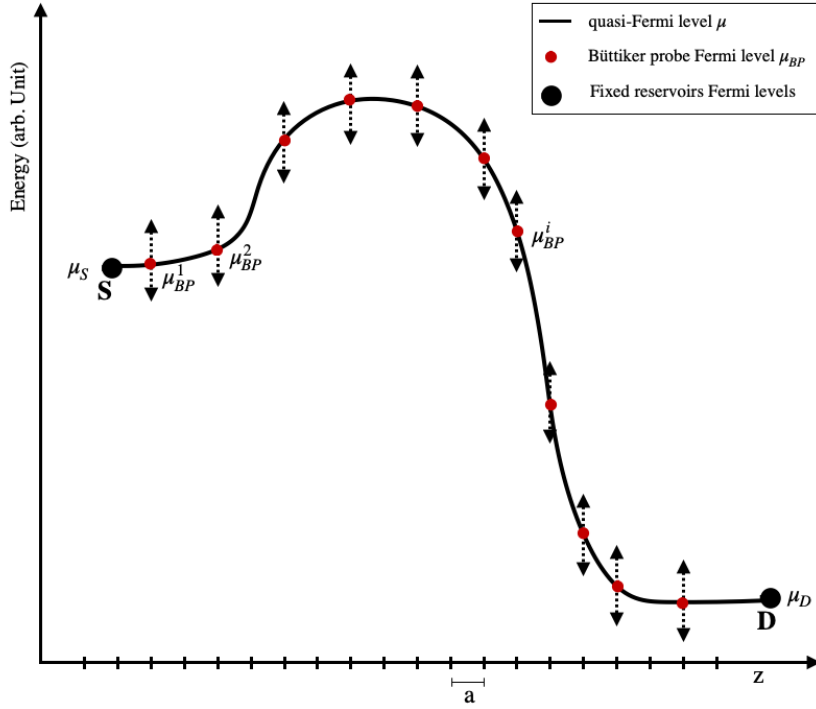


FIGURE 2.4: Schematic representation of the selection of the Büttiker probes Fermi levels at each  $i$ -th point of the discretized domain. Red dots are the position of probes in space while the dotted arrows represent how the value of their associated Fermi level can be shifted in order to achieve current conservation. The black dots are the Fermi level of Source (S) and Drain(D) that must not vary.

The retarded Büttiker probe combines all intra-band scattering processes, such as scattering on various phonons, impurities, and electron-electron scattering into the empirical scattering parameter  $\eta$ , this is a phenomenological parameters related to the bulk scattering time  $\tau$  by the relation [18]:

$$\tau = \frac{\hbar}{2\eta} \quad (2.53)$$

Therefore,  $\eta$  is introduced in the total retarded self energy by defining a self energy Büttiker matrix  $\Sigma_{BP}^R$ . The element of this matrix reads as:

$$\Sigma_{BP}^R(z, z', E) = \delta(z - z') \cdot \eta a \quad \text{if } E \geq E_C \quad (2.54)$$

the parameter  $\eta$  defines the strength of the scattering and has a dimension of an energy, the parameter  $a$  is the mesh step in the discretization of the domain. Within this formalism total retarded self-energy matrix is a diagonal matrix derived from the sum of three contributes, the left and right contact reservoir, and the Büttiker probes.

### 2.4.3 Fermi function

As already explained, the physical observables can be derived by the lesser Green's function, which can be calculated from the greater and lesser self-energy. These two matrices can be derived by the retarded and advanced function by putting eq.(2.51) into eq.(2.50). If a ballistic simulation is considered ( $\eta = 0$  eV) the  $\Sigma^<$  is a sparse matrix with non null terms only at the two vertex, due to the presence of reservoir. So in this case the only used Fermi levels are those fixed by the contacts ( $\mu_L$  and  $\mu_R$ ). As soon as the Büttiker probes are introduced, the self-energy is no longer zero on their diagonal element and a  $f_{FD}$  should has to be calculated on these points.

As stated above, the NEGF model is used to provide a comparison both at equilibrium and out of it, the introduction of Büttiker probes has further increased the complexity of the implementation of the model especially out of equilibrium. In this condition, it can be noticed that is computationally impossible to consider the integral over the discretized space  $k$  directly as is expressed in eq.(2.52), this is caused by the requirement of an iterative procedure to determine the Fermi level developed to ensure the current conservation. On the other hand, this Fermi Level at equilibrium can be considered identically zero and it is still possible to consider the dependence on the wave vector if the length of the device is acceptable. So the implementation of the NEGF approach at equilibrium and with an applied bias will be slightly different, in the following the main differences will be underlined.

### 2.4.4 Equilibrium

At equilibrium, both the Schrödinger model and the localization landscape theory can be used to simulate the device in the study. Here it has been also described how the NEGF approach can be used as a further comparison for the obtained results.

The retarded Büttiker self-energy used for calculating the lesser Green's function at each iteration is written in eq.(2.54). Within this formalism, it is possible to derive all the spectral physical quantities in interest, such as the spectral electron density or the local density of states. Schrödinger or landscape potential are not able to simulate such spectral quantities so in order to have results comparable with these models the spectral density coming from NEGF simulation should be integrated over the energy domain .

As an example the calculation of the electron density [13] has been reported here:

$$n(z) = \int \frac{dE}{2\pi} n(z_i, E) \simeq \frac{\Delta E}{2\pi} \sum_j n(z_i, E_j) \quad (2.55)$$

An other important result that can be extrapolated by this analysis is the local density of state, from which is possible to calculate the integrated density of state (IDOS) already discussed for both landscape and Schrödinger models.

Similarly to what has been done for the electron spectral density is possible to define the spectral density of state as:

$$\text{LDOS}(z_i, E) = 2 \frac{\Delta k}{2\pi} i \sum_{k_j} k_j \cdot [G_{i,i}^>(k_j, E) - G_{i,i}^<(k_j, E)] \quad (2.56)$$

In order to provide a coherent comparison w.r.t. the calculation described in the previous sections, the integrated density of state should be calculated from this latter expression; The IDOS( $E$ ) counts the number of states available under given energy and it is a dimensionless number, as a first glance one can think that these quantities can be calculated just by integrating the eq.(2.56) over the spatial domain. But by doing so the obtained result has a physical dimension of  $[\text{J m}^2]^{-1}$ , that is equal to the physical dimension of a 2D local density of state. It is possible to notice that by doing this integration, it has been consider all the states under a given energy in the studied device, but the desired quantity is the number of states along the direction of confinement (in this case  $z$ ) so the total local density of state should be divided by the constant local density of state of a 2-dimensional not confined system equal to [8] :

$$\text{LDOS}_{2D} = \frac{m_e^*}{\hbar^2 2\pi}$$

here the spin degeneracy has not been introduced because it is already been considered in the eq.(2.56), so the 1-dimensional LDOS that have to be integrated is:

$$\text{LDOS}_{1D}(z_i, E) = 2i \frac{\Delta k}{2\pi} \frac{2\pi \hbar^2}{m_n^*} \sum_{k_j} k_j \cdot [G_{i,i}^>(k_j, E) - G_{i,i}^<(k_j, E)] \quad (2.57)$$

The integration has been performed numerically and it can be shown the obtained results is a dimensionless number as expected.

It is important to notice the IDOS can be calculated only and only if the integration over the discretized  $k$ -vector domain is performed. As soon as the analytical integration is introduced in the model all this kind of information is lost, and the obtained Local density of states is the one calculated for  $k = 0$ , useful for mini-band definition.

### 2.4.5 Analytical integration of transversal wave-vector

Before going on the description of the procedure, the analytic integration of the transversal wave-vector  $\vec{k}$  has to be introduced. This procedure is needed in order to reduce the simulation time when long devices or out of equilibrium simulations are performed. With the aim to eliminate the dependence on this parameter, the sum over all the possible value of  $k$  in eq.(2.52) has to be replaced by an analytic evaluation of the integral. To do so, all the dependences on the transversal energy component have to be moved into the Fermi function  $f_{FD}$ , and then integrating it:

$$F_{FD}(E, \mu) = \sum_{\mathbf{k}} f_{FD}(E + e_{\mathbf{k}} - \mu) = \frac{m^* k_B T}{\pi \hbar^2} \ln \left( 1 + \exp \left( \frac{\mu - E}{k_B T} \right) \right) \quad (2.58)$$

Introducing this result in eq.(2.50) is possible to remove the dependence on  $k$  even for the derivation of physical observables. This approximation introduces a huge save of simulation time, it has been seen that in the equilibrium case in a NEGF simulation both the energy domain and the transversal wave-vector are discretized with a different number of point,  $N_E$  and  $N_k$  respectively, for each value of Energy the above-defined matrices should be calculated for each value of  $k$  leading to a total number of iteration equal to  $N = N_E \cdot N_k$ , by introducing the analytical integration over  $k$ , the total number of iteration  $N$  is simply equal to  $N_E$  speeding up the whole simulation. It is important to notice that without this approximation the numerical evaluation of the Jacobian defined in appendix A would be impossible.

On the other hand, the introduction of this analytical integral does not longer allow expressing the Büttiker as defined in eq.(2.54), because the dependence on the energy  $E$  at which the electrons are injected into the device from the contacts have been lost. Therefore, it is not possible to build up a  $\Sigma_{BP}^R$  that depends on energy, but it has to be defined constant on the whole energy domain. As it has been described in the following chapters this could lead to an overestimation of charges in determining regions, but do not change significantly the current calculation.

## 2.5 Out-of-equilibrium

Now it is possible to define the implementation done in order to achieve a self-consistent solution for the scattering Fermi level introduce in the Büttiker probes.

First of all, the function that has to be minimize have to be defined, within the round-trip approach the spectral current derivate w.r.t. to the coordinate  $z$  can be written as:

$$\frac{\partial J}{\partial z}(E, z_i) = \frac{q}{\hbar} [HG^<(E) - G^<(E)H]_{i,i} \quad (2.59)$$

Where the subscript  $(i, i)$  means that only the diagonal elements have to be considered, furthermore all the dependence on  $k$  has consider with the approximation previously described.

By integrating eq.(2.59) with respect to energy is possible to obtain the current derivate eq.(2.60), this formula is the starting equation used to determine  $\mu_{BP}$ , by imposing that in each point of the domain eq.(2.60) is below a certain small threshold.

$$F(z_i, \mu_{BP}) = \frac{\partial J}{\partial z}(z_i) = \frac{\Delta E}{2\pi} \sum_j \frac{\partial J}{\partial z}(E_j, z_i) \quad (2.60)$$

At the first glance, the problem that has to be resolved in order to ensure the current conservation seems to be similar to the minimization problem defined for the previously describe iterative procedure. However a deeper analysis shows that the function defined in eq.(2.60) does not depends explicitly on the unknown  $\mu$ , and so the Jacobian needed for the implementation of the Newton method can be defined analytically. A possible solution to overcome this problem is to define the Jacobian by means of a numerical procedure, a proper description of this technique and a possible improvement by means of the Broyden method has been reported in **appendix A**.

Finally, with this procedure is possible to determine the Fermi levels that ensure the conservation of the current, knowing them all the wanted physical quantities can be derived and used to compare with the landscape model, unfortunately by introducing the analytical integration over the wave-vector a the physical quantities are calculated for  $k = 0$  leading to a loss of information in the spectral quantities.



## Chapter 3

# Equilibrium simulations

In the following chapter, several structures have been studied at the equilibrium condition, in order to demonstrate the power of the localization landscape model.

In the first case, a quantum well has been taken into account. A quantum well (QW) is a heterostructure with a nanometric dimension, where due to an energy gap mismatch the potential seen by carriers is not uniform inside the structure but depends on the mismatch between the two different values of the energy gaps. QW is the simplest geometry where has been observed quantum confinement and the discretization of the allowed energy levels. Within these levels, a particle is free to mode along the two transversal directions but it is confined along the z-coordinate. Usually, the thickness of the confinement region should be lower than a few nanometres in order to be smaller than the de Broglie wavelength of the carriers. For following analysis a layer of GaAs 2 nm wide has been sandwiched between two long (40 nm) resistors made of  $\text{Al}_x\text{Ga}_{1-x}\text{As}$ . For these simulations, the molar fraction has been modified between 0 and 0.5 in order to study how the LL model behaves for different height of the potential barrier. A schematic view of the described device is depicted in fig.(3.1).

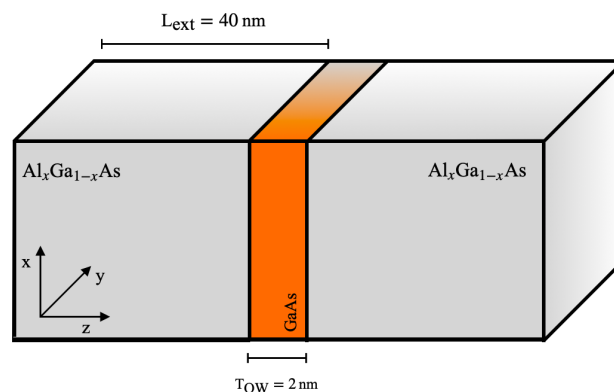


FIGURE 3.1: Schematic backbone of quantum well used in the simulation

This quantum well has been analyzed only at equilibrium condition, and without solving the Schrodinger-Poisson problem, by doing so the charge effects at the hetero-junctions are neglected obtained a flat conduction band.

Then, a more complex device has been simulated, a **superlattice**. Just as a reminder, a superlattice (SL) is a periodic structure of layers of two or more materials, one of the two has a high energy bandgap while the other, where the confinement arises, is characterized by a lower band gap value. Similarly as before, GaAs has been chosen as the low bandgap material and  $\text{Al}_x\text{Ga}_{(1-x)}\text{As}$  as the one with a higher band gap. Dissimilar to the QW analysis the molar fraction has been taken as constant and equal to  $x = 0.5$  for all the simulations. Furthermore, the thickness of confinement regions has been taken as constant and equal to  $T_{\text{well}} = 2.5 \text{ nm}$ , on the other hand, the width of the barriers  $T_{\text{barrier}}$ , that determines the coupling between wells in the active area of SL, has been varied in order to understand how the landscape potential predicts those effects. For this analysis a 31-periods superlattice has been considered, this means that there are 31 wells inside the active region and each of these is separated one from the others by a barrier of thickness  $T_{\text{barrier}}$ .

Moreover, for a particular set of simulations, the positional disorder has been introduced in such structures. The implementation of such phenomena has been described formally in the presentation of the associated results. Finally, similarly to the QW case the active region been sandwiched between two bulk resistors of width 40 nm, which are the Source and Drain contacts. A schematic view of the considered perfectly periodic superlattice has been depicted in fig.(3.2).

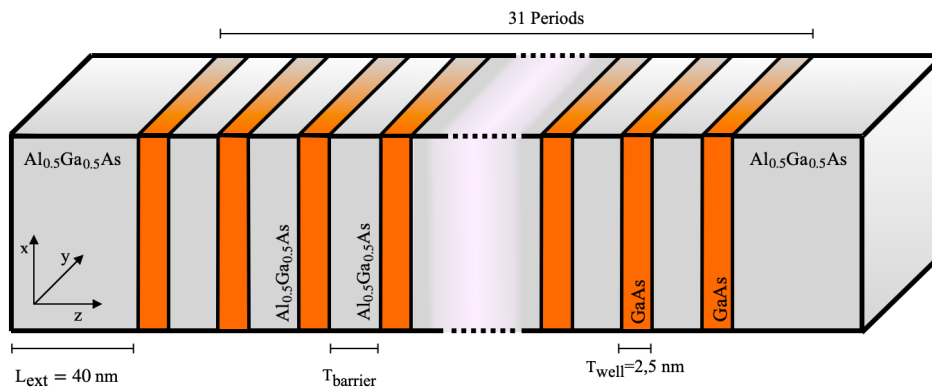


FIGURE 3.2: Schematic view of superlattice structure used in the simulation

Before going on, it is important to recall that the GaAs and AlGaAs has been considered as perfectly lattice-matched, and furthermore, the dispersion relation of electrons and holes have been described with a parabolic approximation with an effective mass constant for both the two material, independent on molar fraction, and equal to the one of GaAs.

For all the described structures the used approach is almost the same: the device is defined as a discretized domain along the  $z$  direction where for each node physicals materials parameters have been defined. Then after having created the backbone of the structure, an initial guess potential is calculated from the neutrality condition and introduced in the self-consistent Poisson-Schrödinger solver explained in sec.(2.1). By solving iteratively that procedure, it is possible to obtain the shape of the potential  $\phi$  from which is possible to calculate the conduction band edge with the following relation:

$$E_C = -q\phi + \frac{E_G}{2} + \chi + \frac{k_B T}{2} \ln\left(\frac{N_C}{N_V}\right) \quad (3.1)$$

Now, the found conduction band  $E_C$  is introduced in the landscape model, where none iterative upgrade of the potential is done in order to have the same initial condition w.r.t the Schrödinger calculus, then  $E_C$  is also introduced in the NEGF approach.

All the outcomes of simulations are stored and post-processed in order to obtain the graphs and values that have been discussed in the following lines.

### 3.1 Quantum well

In this first part of equilibrium analysis, the simplest quantum structure is taken into the study: a quantum well. The molar fraction  $x$  of  $\text{Al}_x\text{Ga}_{(1-x)}\text{As}$  can be tuned between zero and one, by doing so it is possible to change the mismatch in band gap values ( $\Delta E_G$ ) leading to a different confining potentials. Anderson's rule has been used to determine how  $\Delta E_G$  is separated between the conduction band offset ( $\Delta E_C$ ) and valence band offset ( $\Delta E_V$ ). It is known that the energy gap is the difference between the lower edge of the conduction band and the upper edge of the valence band, hence by aligning the vacuum levels of the two materials (Anderson' rule) it is possible to write, for two semiconductor labeled as 1 and 2:

$$\Delta E_C = \chi^2 - \chi^1 \quad (3.2)$$

where  $\chi$  is the electrical affinity. Similarly the valence band offset can be defined as:

$$\Delta E_V = E_G^2 - E_G^1 - \Delta E_C \quad (3.3)$$

By looking at the material parameters, it can be seen that the affinity of GaAs is fixed while the one of AlGaAs depends on the molar fraction ( $x$ ). By substituting those values in eq.(3.2) and eq.(3.3) it can be seen that the conduction

band offset depends on the molar fraction too. The analytical function that describes the dependence of the conduction band offset on the molar fraction ( $x$ ) can be derived and written as:

$$\Delta E_C = +0.839x - 1.4370x^2 + 1.310x^3 \quad (3.4)$$

Form eq.(3.4) it is possible to notice that between  $x \in [0, 1]$  the conduction band offset is a monotonic increasing function, so for a higher value of  $x$ , the conduction band offset and therefore the potential barriers seen by the electron increase. It has to notice that this analytical expression has been derived just to give to the reader a quick understanding of the behavior of conduction band offset, but the function used in implementations does not have this form, in order to do not introduce numerical errors. In the table (3.1) has been depicted the conduction and valence band offset for the four different values of the molar fraction used for the following simulations, moreover, it has to be recalled that those values depend neither on the doping nor on the length of the device so they are also valid for the superlattice simulations.

$x$	$\Delta E_C$	$\Delta E_V$	$\Delta E_G$	$\Delta E_C / \Delta E_G$
0.1	0.0713 eV	0.0530 eV	0.1243 eV	57,36%
0.2	0.1218 eV	0.1060 eV	0.2268 eV	53,47 %
0.3	0.1590 eV	0.1592 eV	0.3182 eV	49,97%
0.5	0.2240 eV	0.2650 eV	0.4890 eV	45,81%

TABLE 3.1: Conduction and valence band offset for several values of molar fraction( $x$ )

The sign of the conduction and valence band offset are both positive because a junction between GaAs and AlGaAs is a type-I heterostructure where the bottom of the conduction band and the top of the valence band are formed in the same semiconductor layer (GaAs). In this case, the confinement of electrons and holes arose in the same layer. A higher value of  $x$  determines a bigger barrier seen by electron inside the quantum well leading to higher confinement. Different values of  $x$  have been considered in the following simulation in order to understand if the landscape potential works properly for both high or low confined states.

The first geometry in study is a well 2 nm wide made of GaAs enclosed between two barriers 40 nm wide of  $\text{Al}_x\text{Ga}_{(1-x)}\text{As}$ , the simulations have been performed with four different values of molar fraction  $x = [0.1, 0.3, 0.5]$ . In this geometry doping has been assumed as constant and equal to  $N_D = 10^{18} \text{cm}^{-3}$  additionally the **incomplete ionization** model has been introduced with the aim to describe the activation of doping impurities. Furthermore, the effective mass for electrons and holes have been considered as constant for the whole device and equal to  $m_e = 0.067m_0$ ,  $m_{lh} = 0.090m_0$  and  $m_{hh} =$

$0.349m_0$  these are the electron, light hole and heavy hole effective mass, respectively.

Due to the small total length of the geometry, it possible to selected a fine mesh step so the z-axis domain has been discretized with a mesh step of  $\Delta z = 0.1\text{nm}$ .

The following simulations have been performed just to give a first introduction of the landscape model and to better understand its proprieties, therefore the Poisson self-consistent solution has not been calculated for those simple structures. Hence the landscape method has been applied to a flat band QW, in order to neglect the space charge effects. To do so the potential  $\phi$ , needed to find  $E_C$ , has been considered as constant and equal to the value derived from the **neutrality boundary condition**, then the conduction band edge has been calculated by introducing this values in eq.(3.1).

The Schrödinger equation has been resolved for such distribution of potential for both electrons and holes. From its solution, as it has been described in sec.(2.1), two main outputs are obtained: the set of eigenenergies and their associated wave-functions. Form these it is possible to obtain the electron density and ground state  $E_0$  for the confined states and moreover, the integrated density of states can be derived following the steps described in 2.1.3.

First of all, the conduction band and the associated Landscape potential have been shown for the four geometries in the study, fig.(3.3), this latter potential has been calculated using the conduction band  $E_C$  as the potential  $V$  in eq.(2.29) and proceeding as discussed in 2.2. For those geometries, the minimization of the potential has been done just by putting at zero the bottom of quantum well. As it can be easily seen, the shape of landscape potential is smooth and furthermore, it perfectly matches the conduction band outside the confinement regions. This shape can be better understood considering the eq.(2.29), indeed the inverse of the potential  $u$  is the solution of a differential equation in which a second-order derivative is involved, therefore the function  $u$  is  $\mathcal{C}(z)^2$ , this means that  $u$  is continuous in the interval  $z$ , together with their derivatives of order 2, leading to this a smooth shape. Going on, it is interesting to see that the variation of effective potential  $W_C$  extends far-off the edge of the well, as soon as this potential is introduced in the Fermi function, in order to calculate the carrier densities, it originates two main changes w.r.t the classic calculation: a decrease of carrier densities in the confinement subregions and a smooth transition between well and the external bulk material.

In the same figure (3.3), it is also represented a comparison between the predicted **ground states energies**, the black dotted line is the one found by solving the eigenvalue Schrödinger problem while the red one is the ones found with the LL potential. In order to calculate the confinement energy state the eq.(2.32) has been used as the integration domain,  $\sigma_m$  the whole space  $z$  has been considered, this approximation of  $\sigma_m$  does not seem to overestimate the results. As a first glance, it is possible to see that this new model

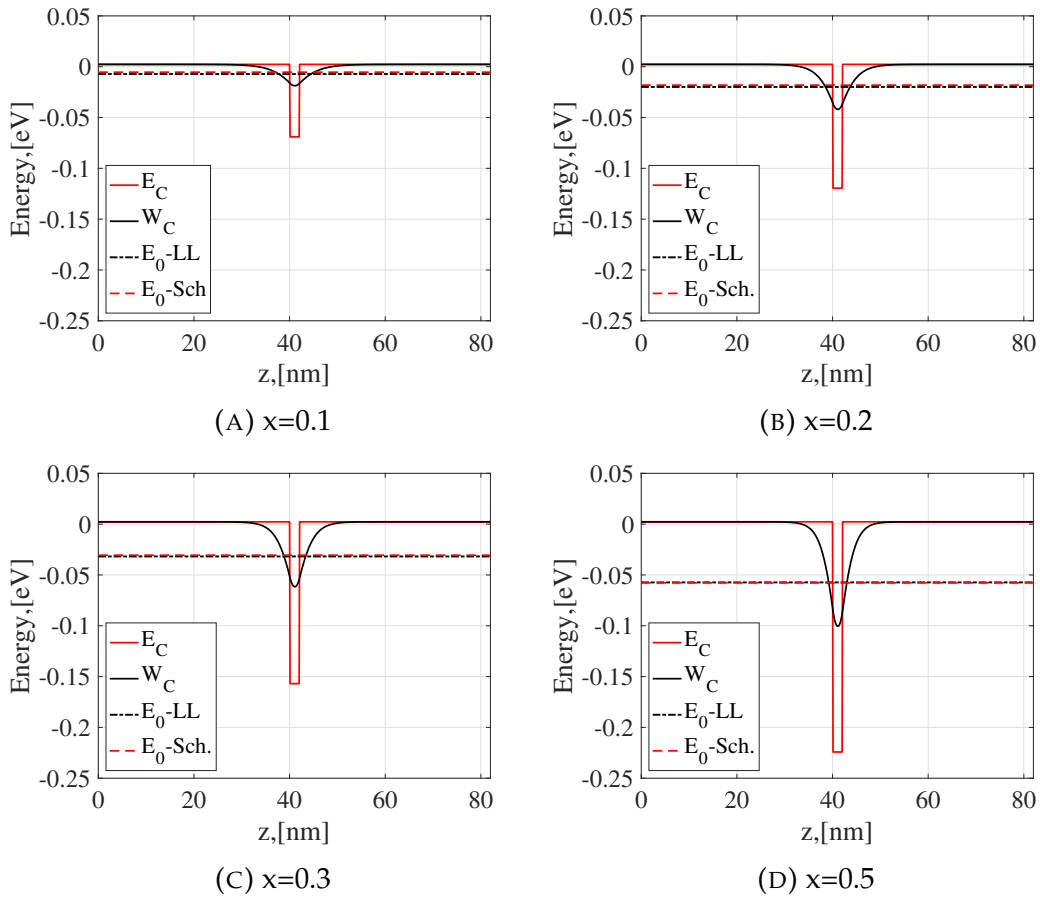


FIGURE 3.3: Comparison between Poisson-Schrödinger conduction band and its associated Landscape potential (solid line), comparison b.t. ground state derived from Landscape approximation and Schrödinger eigenvalue problem, at different values of molar fraction  $x$

exhibits a remarkable agreement w.r.t. the results found from Schrödinger, especially for high confined states ( $x = 0.3$  and  $x = 0.5$ ). A further comparison of these values has been performed in tab.3.2, where also the relative error of LL prediction has been calculated. It has to be notice that the absolute errors between the two results is almost independent of the height of barriers, and the reduction of the relative error can be explained considering that a higher confining potential leads to a deeper ground state energy.

$x$	LL [eV]	Schrödinger [eV]	abs. relative error
0.1	0.006 eV	0.007 eV	16.66 %
0.2	-0.020 eV	-0.018 eV	11.11 %
0.3	-0.032 eV	-0.031 eV	3.23 %
0.5	-0.057 eV	-0.058 eV	1.72 %

TABLE 3.2: Comparison of the ground state energy for different values molar fraction.

Then, the potential  $W_C$  has been introduced in eq.(2.38) in order to compute the electron density in the conduction band. In fig.(3.4) has been depicted as a comparison between the results obtained from four different methods (classical, NEGF, LL, Schrödinger).

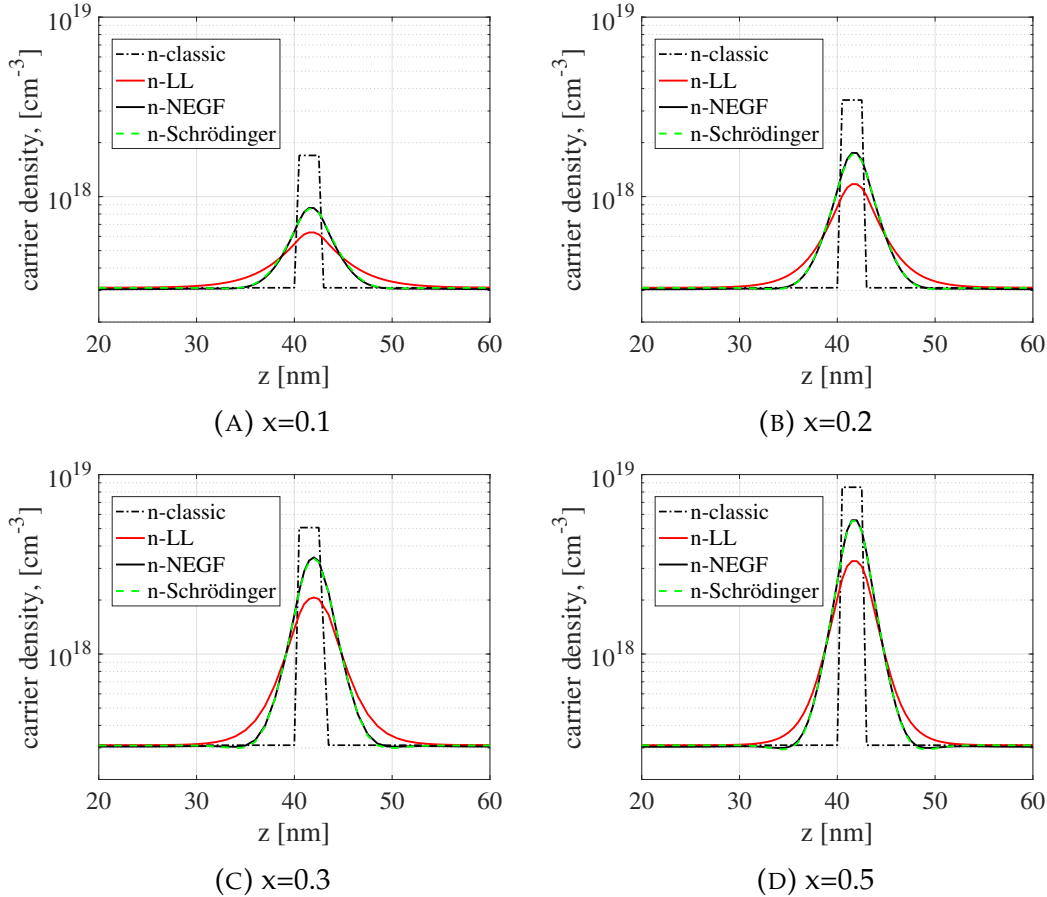


FIGURE 3.4: Electron density, calculated for the four different methods compared to the classical one, at different values of molar fraction  $x$

At a first glance, it is easy to notice that the classical results are close to the Schrödinger, NEGF, and LL curves only at the edges of AlGaAs, where no quantum effects are present. In fact, inside the well, the classical results are almost constant and highly overestimate the carrier densities, then they drop sharply outside the well, not accounting for the quantum nature of the electron. In the following results, the classical calculation has been always depicted in order to provide a further term of comparison, but for sake of simplicity, it has been no longer commented on, due to its inability to consider quantum effects.

Going on, the electron density calculated with the LL model perfectly matches the other curves in the bulk region, where the effective potential is equal to the classical one. In fact, far away from the well, no quantum effects are present, and the two models are perfectly coherent. By getting closer to the well, it is possible to observe that the other curves pull away from the classical

one at distance from the well almost independent of the height of the barrier. Furthermore, it is possible to notice that this length, where the quantum effects start to affect the electron density, is bigger in the landscape model. A possible explanation for this effect is that this new effective potential  $W_C$  slightly overestimates the tunneling of states from the barrier. This consideration has a further proof if a comparison between the peaks inside the well is provided. Indeed, it is possible to see that the absolute value of electron density in the well, calculated with the landscape model always underestimates the carriers. Therefore, the effective potential found by the LL model inside the confinement region is barely too small, leading to a tunneling effect higher than the one predicted by the Schrödinger simulation. Finally, it can be noticed that the results predicted by the NEGF and the Schrödinger method are perfectly coincident, for these simulations the integration over the discretized wave-vector domain is still taken into account so it is also possible to calculate the IDOS.

Finally, the integrated density of state (IDOS) has been analyzed, the obtained comparison between the four models in analysis has been depicted in fig.(3.5). As expected, the Schrödinger integrated density of states is a step function where for each value of eigenenergy the IDOS counts two states (the number of states inside the well multiplied by the spin factor), instead the other two quantities, by definition, have to be continuous.

For high values of energy, the IDOS behaves as a bulk one, following the **Weyl's** asymptotic law. The IDOS calculated from the original potential  $E_C$  matches the other simulations only at high energy but totally fails the description at lower energy, with a take-off energy too small, equal to the bottom of the conduction band. On the other hand, by considering LL approach it is possible to see that the take-off energy shifts to higher values due to the introduction in the simulations of quantum effects. Going into detail, it is possible to observe that in the LL model the IDOS become different from zero about 10 meV before the Schrödinger curve, this behavior can be explained considering the definition of IDOS in eq (2.40), this is a continuous function so in order to reach a certain high for given values of energy it has to detach at a smaller value of energy w.r.t. a step-wise function obtained from Schrödinger eq.(2.26)), [8]. A similar behavior it is also observed in the NEGF's IDOS, especially for low values of confining potential but on the other hand, better predicts the results in the confinements region. At higher energy, the reason for the jagged shape of the IDOS can be attributed to the discretization of transversal vector  $k$ .

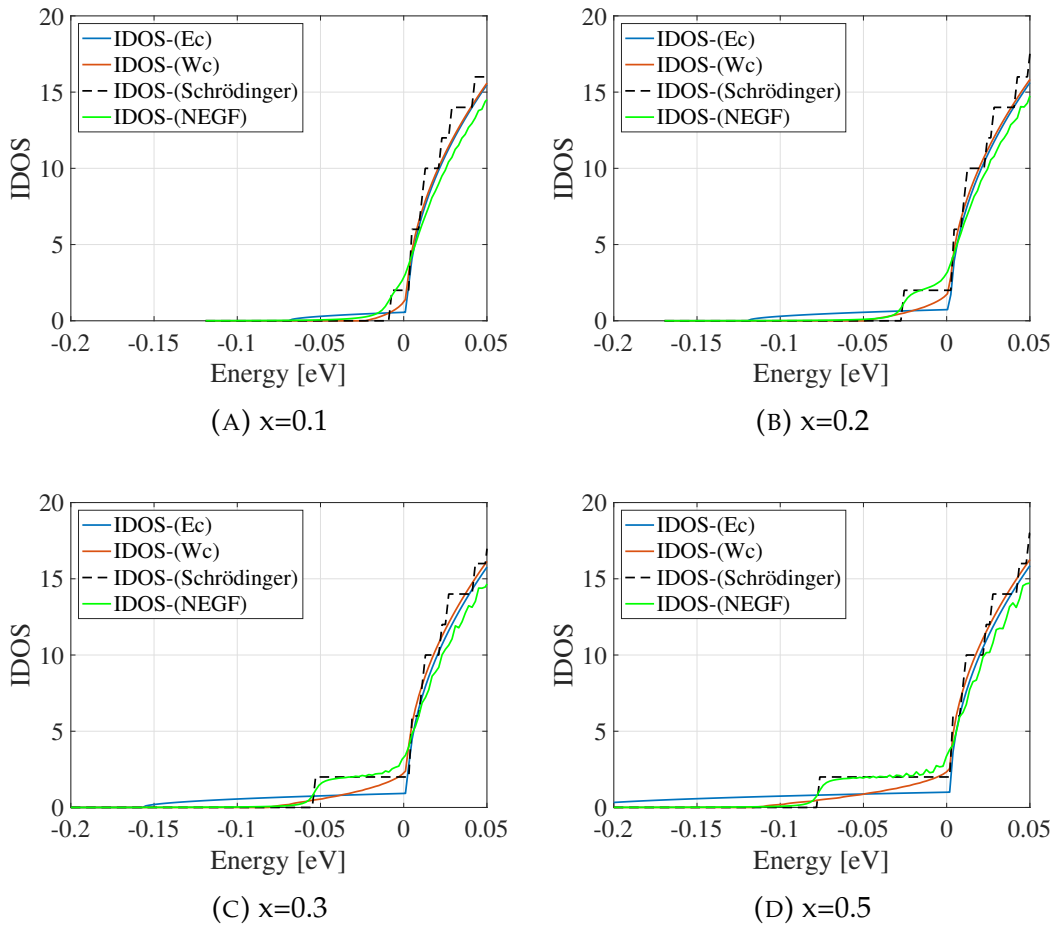


FIGURE 3.5: Integral density of states, calculated for the four different methods, compared to the classical one, at different values of molar fraction  $x$

## 3.2 Superlattice

In this section, a different kind of geometry is taken into account, a superlattice (SL). This device constituted by periodic structure is widely used in commercial application as for example LEDs or other optical devices, like brag mirrors or photodetectors.

An SL is mainly a periodic structure of two or more materials and it can be considered as a periodic replication of the quantum wells described above. The first distinction between superlattices can be performed by considering the width of barriers  $e$ , in fact, if this length is small it possible to talk about a **coupled superlattice** or simply a superlattice while on the other hand a **low coupled superlattice**, or multiple quantum wells, is characterized by wider barriers. Both of these two cases have been analyzed in order to understand if the ,landscape model is able to describe such structures.

Then the effect of **position disorder** has been considered on those superlattices, where further effects of localization can occur due to the Anderson theory.

### 3.2.1 Periodic Superlattice

The first geometry considered is a 31-pairs of GaAs/AlGaAs hetero-junction sandwiched between two bulks AlGaAs. The whole structure has been doped by an constant donor dopant density equal to  $N_D = 10^{18} \text{cm}^{-3}$  and the effective mass has been considered as constant and equal to the GaAs bulk effective mass.

The simulations have been performed for four different values of barriers width while the wells regions have been left unmodified. Those thickness have been varied between 10 nm and 2 nm in order to account all the possible coupling condition, ranging respectively from a low coupling condition to an high one.

The external bulk length has been imposed equal to  $t_{bulk} = 40 \text{ nm}$ , the mesh step has been increase to half a nanometres ( $\Delta z = 0.5 \text{ nm}$ ), while as molar fraction of  $\text{Al}_x\text{Ga}_{1-x}\text{As}$  the value  $x = 0.5$  has been selected, in such condition by following the results depicted in table 3.1 the confined potential for the electron, in the wells regions, is equal to 0.2240eV.

Furthermore, for these simulations, the NEGF approach has been slightly modified with respect to the quantum well case. Due to the higher length of the device, computation time has greatly increased. Hence the analytical integration over the wave-vector  $k$ , explained in 2.4.5, has been introduced. It has to be further notice that, even if the simulation time is still achievable, at least at equilibrium, this integration was mainly introduced in order to provide a perfect matching between the simulations performed at equilibrium and out of it, indeed in the latter, it is impossible to consider the numerical integration over the  $k$ -domain. As already explained, all the physical quantities that depend on the components of transversal wave-vector, as for example the LDOS, has been lost, and that why in the following result the NEGF's IDOS has not been depicted.

First of all, the four different conduction bands in the active region of SL have been depicted, in fig.(3.6), with their associated effective potentials. It has to notice that the total length of the devices is different in the four cases, but in order to provide an immediate comparison only two dozen periods have been depicted and furthermore, the four plots have all the same energy ( $y$  - axis) scale. Usually, the devices based on SL are very long, some  $\mu\text{m}$  as for example in photodetectors, so the most important results are those in the middle of the periodic region where the conduction band is not affected by edges and by the space charge bending. For these reasons the following results has been presented only in this region, according to the geometry taken into study different parts of the device is considered.

It easy to understand that, by increasing the width of barriers the landscape potential approaches the classical one in the barriers region, this is because the quantum effects are weaker and the tunneling between wells is reduced, as it can be easily seen in fig.(3.6d) or fig.(3.6c) the potential seen by the electron in the confinement region increases by increasing the barriers width. By contrast, if small barriers (3.6a and 3.6b) are simulated, the effective potential

is quite different from the conduction band edge, this effect can be explained by considering the coupling among wells. In fact, the tunneling between two confined states effects is higher when the thickness of barriers is small, due to a higher overlap of the tail of wave functions. By studying those graphs, it is underlined how this new effective potential is capable of reducing the barriers seen by electrons in the confinement regions just by introducing in an effective way quantum tunneling. By comparing fig.(3.6a) and fig.(3.6d) is possible to see that an electron inside an inner well sees a dissimilar value of confining potential, even if the height of classical barrier is the same.

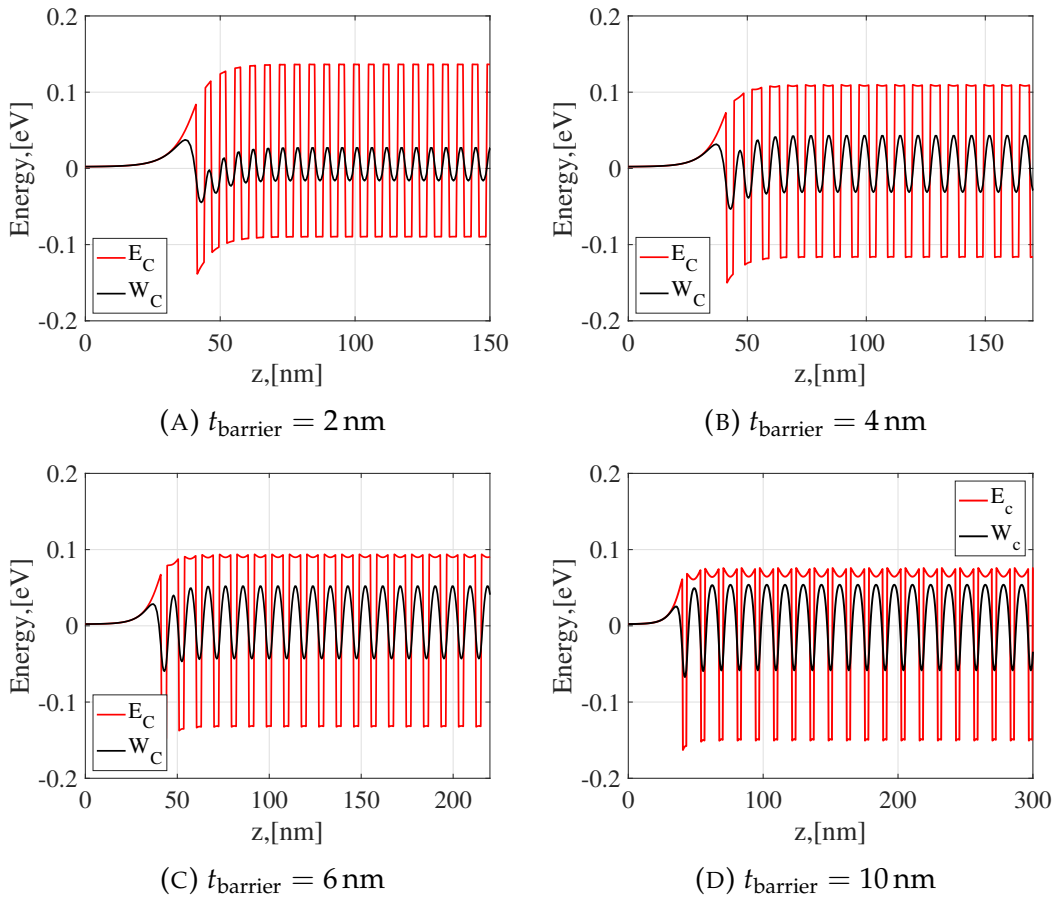


FIGURE 3.6: Portion of conduction band, for the four different values of barrier width, with the associated effective potential ( $W_C$ ) found with Landscape model.

Then the behavior of the valence band has been analyzed, valence band edge has been derived from the obtained conduction band described above simply subtracting the non-continuous value of energy gap  $E_G(z)$ .

$$E_V(z) = E_C(z) - E_G(z)$$

The obtained results have been sketched in fig.(3.7) where the energy scale on the ordinate is equal to the one used for the conduction band, in order to perfect compare the two outputs of simulations.

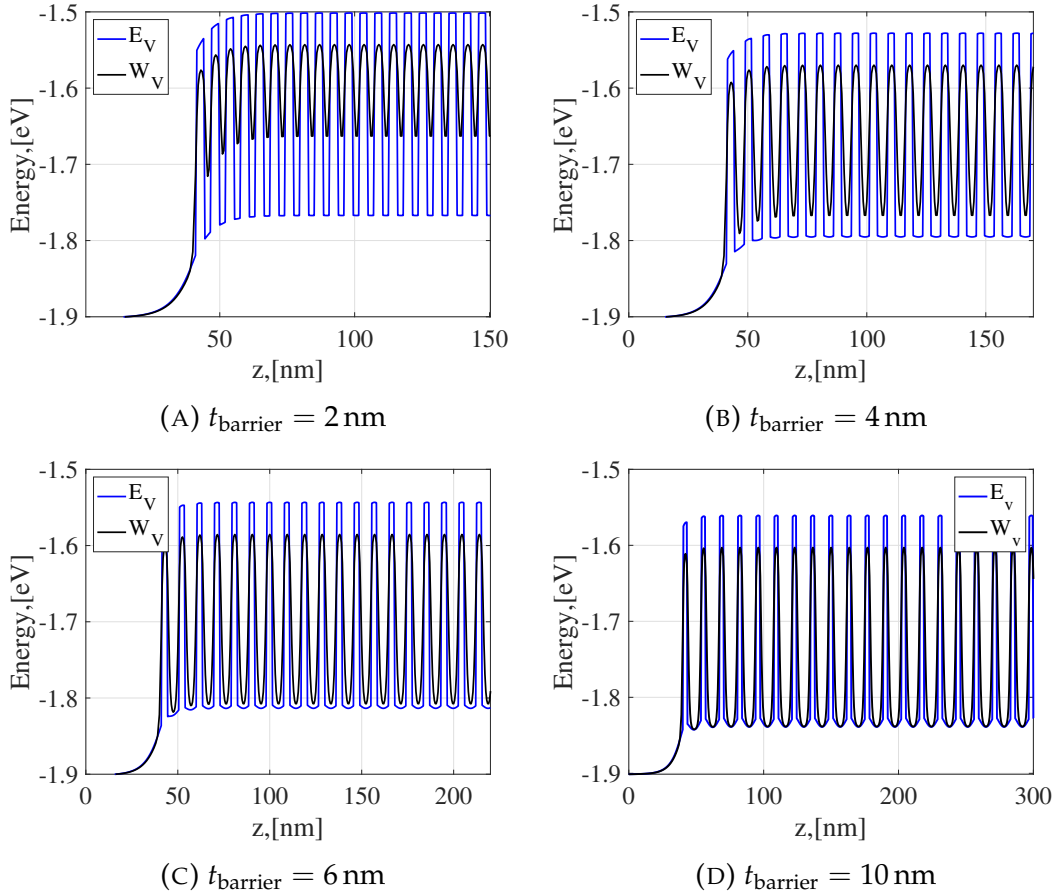


FIGURE 3.7: Portion of valence band, for the four different values of barrier width, with the associated effective potential ( $W_V$ ) found with landscape model.

It can be noticed that the landscape potential behaves differently in the valence band. Even if the holes confining potential is slightly higher than the one of the conduction band ( $\Delta E_V = 0.2650\text{eV}$ ), the landscape potential is closer to the classical one even with small barrier width. The reason for this behavior can be imputed to the higher value of holes effective mass. First of all, a higher mass will lead to a lower ground state energy and a higher number of allowed states in the well, leading to a potential  $W_V$  close to the bottom of the well. On the second hand, by recalling that the tunneling probability decreases exponentially with the mass, holes will have a lower probability to escape from the well, and they saw a potential that is very close to the classical one.

Then, in order to better understand the confinement of states in those superlattices, the IDOS, the integrated density of available states, has been calculated with the same approach used for the quantum well, obtaining the results shown in fig.(3.8). For very low coupling between the wells, the IDOS increased through a series of steps fig.(3.8d), it can be demonstrated that the first two steps have a height equal to 4, this is because due to band bending and charge effects the two nearest well to the contacts have different shapes

and ground states energy with respect to the ones in the flat portion of conduction band. Then the IDOS shows a big step of height 58 that is equal to the numbers of wells in the flat band regions multiplied by the spin factor, reaching the value of 62 that it is double the periodicity of the multiple-QW. This behavior can be explained considering the degeneracy in energy level inside the wells: due to low coupling, the wells behave as a set single quantum wells with all the same ground state leading to this stepwise shape of the IDOS. This step-wise behavior of IDOS is also present in the case depicted in fig.(3.8c), in which the transition is not so sharp due to an increased coupling between wells.

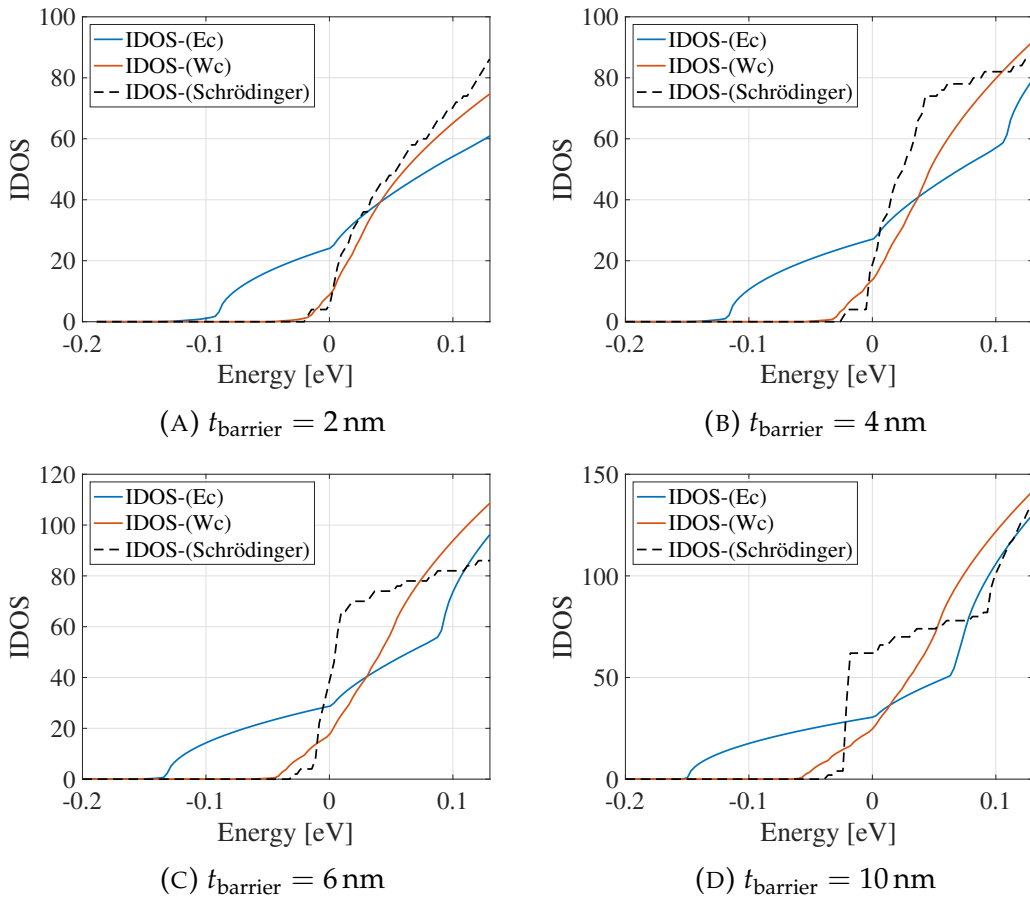


FIGURE 3.8: Comparison of the Integrated density of states, calculated with the three different approaches, for distinct barriers width

On contrary, in fig.(3.8a) the IDOS presents a smoother shape, in fact here the SL can not be considered anymore as a set of single QW due to higher coupling between them. In this case, the degeneracy is lifted and the mini bands arise. Therefore the IDOS grows with small steps of height 2 that are not perceptible in the scale of the graph. Due to this smoother behavior the LL prediction of the IDOS is almost coincident to the one obtained with Schrödinger and entirely match the lift-off energy. On the other hand as soon as the degeneracy of state increases, the continuous landscape prediction is not able to follow such a stepwise function so the results are quite different,

even the lift-off energy starts earlier. At higher energy (more than 100meV) the states are no longer confined so the IDOS follow Weyl's asymptotic law and the three results are equivalent.

Finally, it is possible to state that the landscape prediction of the IDOS perfectly matches the Schrödinger results, if a coupled superlattice is taken into study, while, it is still not able to follow a step-wise function, but it provides strongly preferable results than the classical prediction.

Subsequently, the carrier densities have been analyzed. The results have been depicted in fig.(3.9). As already said the region of interest is the central part where the edge effect is negligible and the conduction band is flat, so about ten periods of these SLs are depicted, moreover the results are sketched with the same logarithmic scale in order to immediately appreciate the differences.

At a first glance, it is possible to see that for higher barriers the electron density in the confinement regions is bigger than the one with a lower width of barriers, this is because, as already explained, a bigger barrier reduced the tunneling between wells, reducing the rate of electrons that can escape from the barrier due to tunneling.

Going into details, it is also possible to see that the landscape model properly describes the carriers inside barriers, the relative error between the peaks is always lesser than 10 % for all geometries in the study. While the main differences are inside the wells, similarly to what has been discussed in QW analysis, the landscape works better when the state is not so confined, in fact, is possible to show that the relative error in the peaks of electron density inside the well is about 30 % in fig.3.9c and decrease to less than 8 % for the fig.3.9a. Similarly, to what has been described for the IDOS the LL model seams predicts better results for coupled SL.

Furthermore, by studying fig.(3.9) it is possible to see that the NEGF approach slightly overestimates the carrier densities, especially in the barrier regions. This effect has one main reason, that can be explained by recalling the definition of the Büttiker probes for those specific simulations: due to the high length of the devices it is necessary to introduce the analytical integration over the  $k$ -space defined in eq.(2.58), this will lead, as already discussed, to a definition of the Büttiker independent on energy, this formalism has the drawback to introducing some centers of scattering even in the forbidden bandgap, by doing so the population of the carriers inside the gap is not identically zero. This approximation of the probes does not affect the calculus of spectral quantities such as LDOS or spectral current density, because the contributes in the bandgap is too small. Therefore as soon as an integration over energy is performed, as for example, in this case, this small contributes can lead to some unwanted effects. This overestimation is negligible in the wells regions because the minima integral domain is very close to the bottom of the well edge.

In conclusion, it has to notice that even for those geometries the classical prediction totally fails the description of such devices.

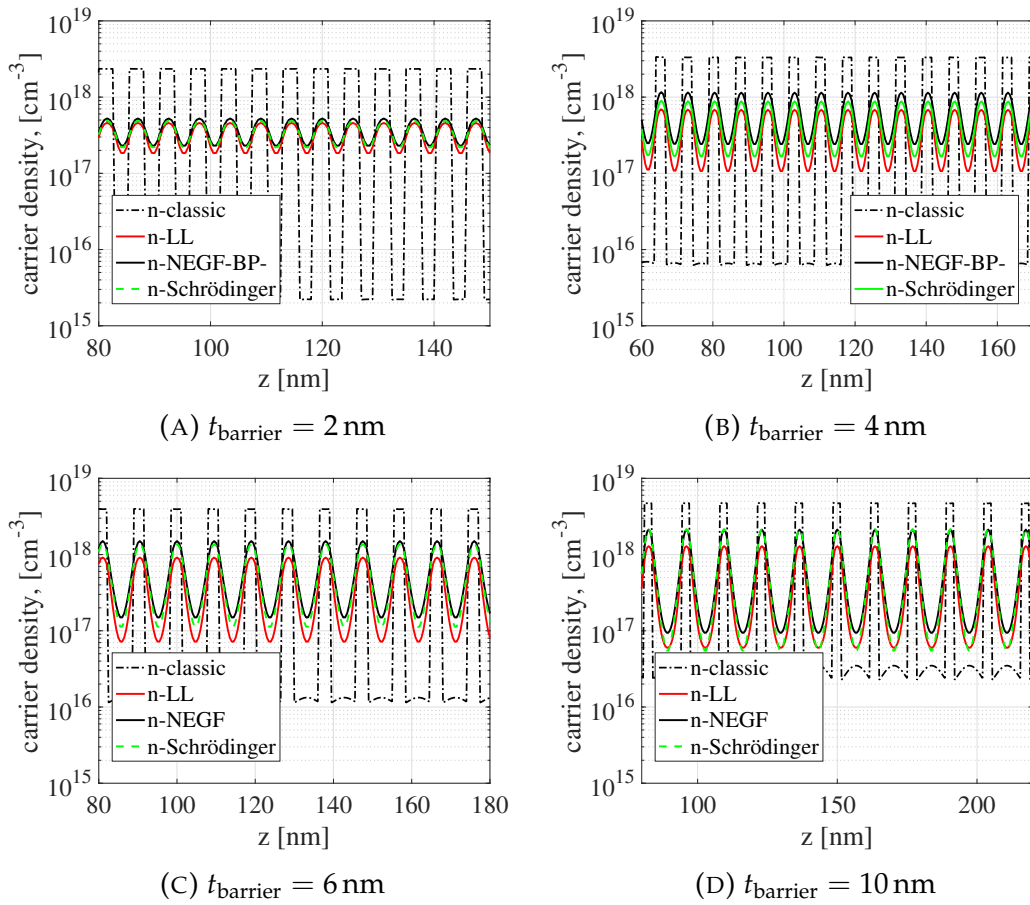


FIGURE 3.9: Comparison of the electron density in conduction band, calculated with the four different approaches, for distinct barriers width.

As an additional test, the pre-discussed LL method has been applied to the valence band in order to obtain the density of the minority carriers. Just as before these results are compared with one found from the Schrödinger-Poisson method and with the classical prediction. The NEGF method has not to be implemented for the calculation of holes in order to not further increase the simulation times.

The obtained output has been depicted in fig.(3.10), the subregion of SL represented is the same used for the presentation of conduction band results. At a first glance, the holes behave as expected, the absolute value of concentration density is very small because the device is n-type and holes are the minority carriers. Furthermore, the holes show strong confinement in the wells due to the higher effective mass. Even in this case the landscape and the Schrödinger results are comparable. It can be noticed that for the two cases with low coupling fig.(3.10c) and fig.(3.10d) the density of the holes approach the classical ones in the middle of barriers regions, meaning that the tunneling between wells of such heavy carriers is negligible for these barriers width.

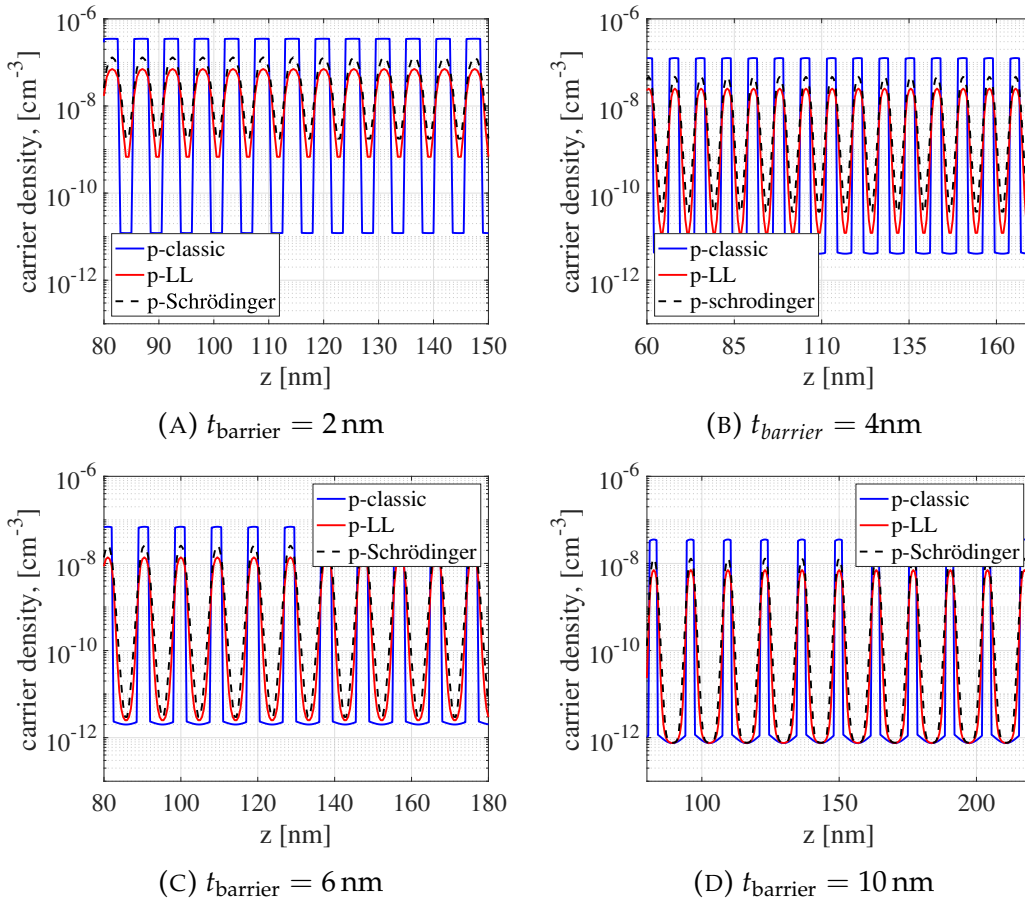


FIGURE 3.10: Comparison of the hole density in valence band, calculated with the three different approaches, for distinct barriers width

### 3.2.2 Disordered superlattice

To further test the LL model, the positional disorder has been introduced in the superlattice. By doing so the periodicity of the SL is no longer constant in the whole device but it has some fluctuation from the original period due to the random thickness of the barriers and wells.

The disorder has been introduced directly in the geometry delineation. It has been assumed that this positional disorder comes from the process of deposition of the layers, by doing so it has been hypothesized that this process is able to deposit a sheet of material with an absolute error of one layer of atoms. The lattice constant of GaAs is  $5.6533 \text{ \AA}$  while the one of  $\text{Al}_x\text{Ga}_{1-x}\text{As}$  is  $[5.6533 + 0.0078 \cdot x] \text{ \AA}$  where  $x$  is the molar fraction. As a first approximation, both values are considered equal to the one of GaAs independently on the molar fraction. On the second hand, it has to be recalled that the space domain has been discretized with a mesh of  $5 \text{ \AA}$ , so this latter value has been selected as the precision of this fictitious deposition process. Under this assumption, the original thickness of a single well or barrier can be increased or reduced by  $5 \text{ \AA}$  with a certain probability. The probability to have a deposition different from the original one has been set to 40% while no distinction is done on the probability to have one more or one less layer. Summing up, the

thickness of a well or a barrier has been described by a uniform distribution where the probability to have the original expected value  $T$  is 60 % while the one of having  $t = T + 5 \text{ \AA}$  is the 20 % equal to the one of having  $t = T - 5 \text{ \AA}$ .

Now it is possible to introduce disorder into the superlattices described in the previous section, for sake of simplicity, in showing the results only two cases are studied, the first one is the high coupled superlattice depicted in fig.(3.6a) while the other is the low coupled case fig.(3.6c).

The new obtained geometries are depicted in figure 3.11, it is easy to notice that the conduction band edge has been reshaped by the disorder and does not have anymore a flat behavior in the active region. Due to not perfect periodicity of superlattice, confinement of carriers depends on the local structure, leading to an irregular shape of the potential  $\phi$  calculated from *Poisson equation*.

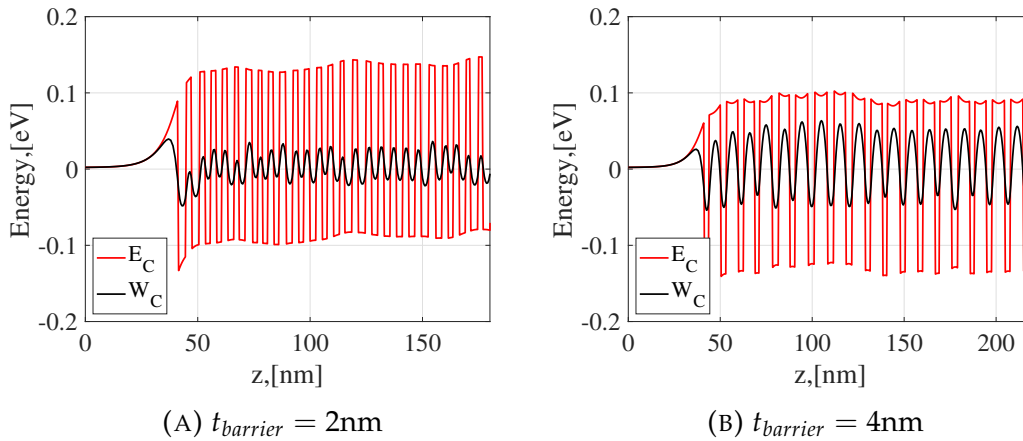


FIGURE 3.11: Portion of conduction band of a disordered superlattice, for the two different average values of barrier width, with the associated effective potential ( $W_C$ ) found with Landscape model

As expected also the shape of effective potential  $W_C$  differs from the previous one, it seems to follow the different strength of tunneling and confining effects by reducing the potential seen by the electron in subregion where the barriers have been shrunk in width, *au contraire* the effective potential has been reduced in subregions where the GaAs (well) has been deposited with one more layer.

Now considering that the landscape model seems to properly take into account the disorder fluctuation of the potential, carrier densities have been calculated and compared to the one obtained with Schrödinger, classical model, and NEGF, the results have been depicted in fig.(3.12).

It can be noticed that the curves derived from the LL theory follow the variation of carriers due to disorder, modeled with Schrödinger approach, in a proper way. The main differences between peaks are in strong localized confined regions where it has already been demonstrated that the LL model underestimates the charge density. Even in these cases, it is possible to see

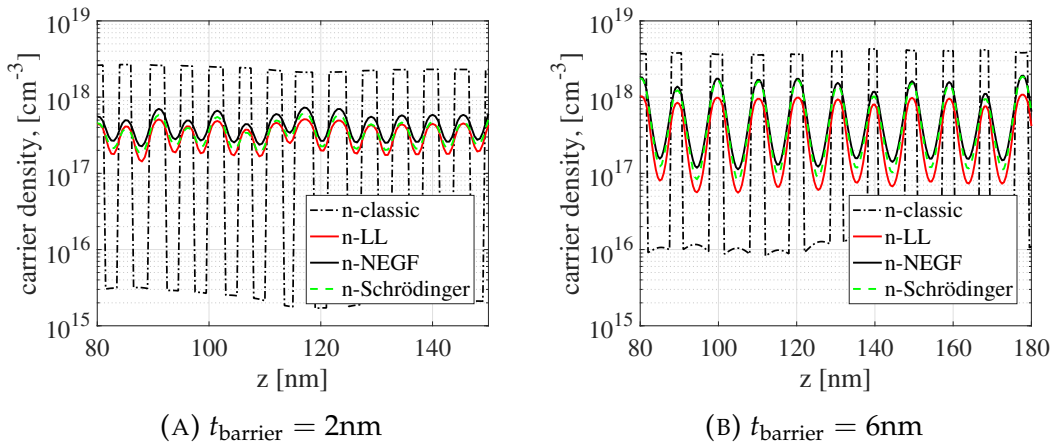


FIGURE 3.12: Comparison of the electron density in conduction band, calculated with the four different approaches, for two distinct barriers width.

the overestimation of the carriers with the NEGF approach.

As a further analysis, the hole density has been sketched in fig.(3.13) with the aim to once again underling the influence that a higher effective mass has on the calculation of the effective potential  $W_V$ .

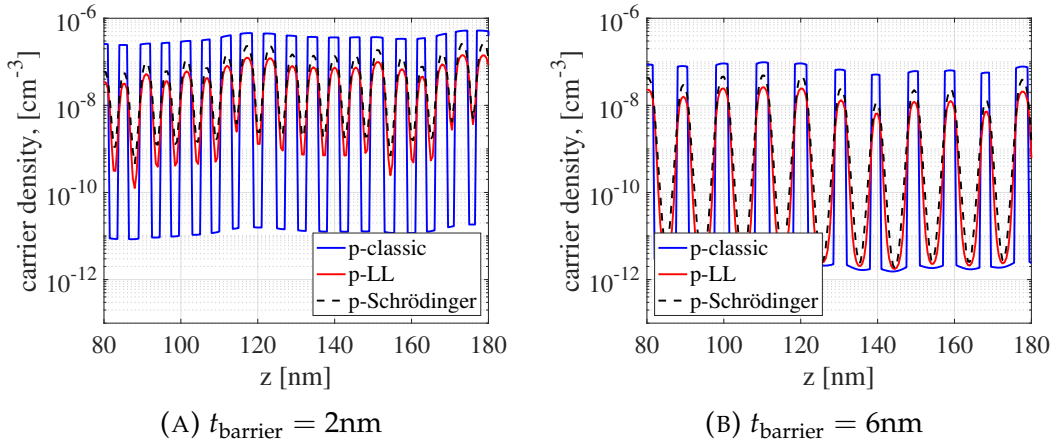


FIGURE 3.13: Comparison of the hole density in valence band, calculated with the three different approaches, for distinct barriers width.

The disorder has been introduced in these simulations with a further aim: understand how a not perfect periodicity changes the transport proprieties especially on the definition of mini-band. All these considerations and extra analysis will be performed in parallel w.r.t. the periodic lattice in the following subsection where the spectral results coming from the NEGF simulation are presented.

### 3.2.3 NEGF simulations

The non-equilibrium Green's function approach is a computation expensive tool but allows to obtain some results that are impossible to achieve with the classical Poisson-Schrödinger solvers or even less with the landscape model. In this section has been presented some meaningful results derived from the NEGF approach, such as the spectral electron density that allows describing the mini-bands formation in the superlattice. Mini-bands are very important in the description of carriers motion in the superlattice, the dispersion relation of the system defines the allowed energy band where the electron flows, this is because the electron and holes are delocalized in the whole region crossed by the miniband.

First of all, the electron spectral density has been depicted in fig.(3.14), in order to understand how the Büttiker probes allow populating the wells regions. It has been demonstrated that without the introduction of these probes the NEGF approach considers the device as a ballistic and therefore a propagator injected from left and right contact is not able to reach energy levels below the Fermi levels of the contacts ( $\mu_R, \mu_L$ ) and so it is impossible to describe the confinement of carriers. The Büttiker probes model introduces a fictitious set of carriers reservoirs inside the device at an energy level lower than the one of contacts, by doing is possible to extract and inject electron in the region not accessible from the contacts. Going into details, within this approach is possible to study the population of carriers due to the scattering events and furthermore the effects of dissipative transport.

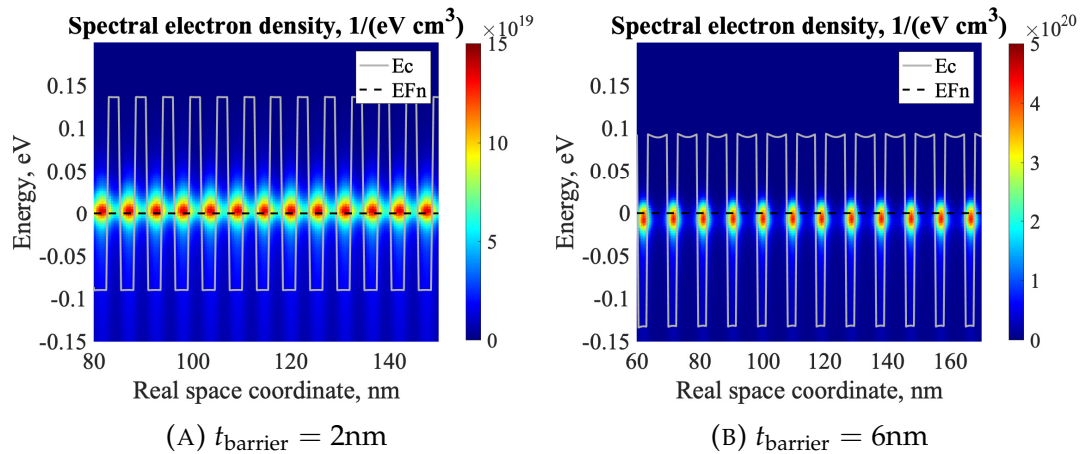


FIGURE 3.14: Electron spectral density depicted for a dozen period in the middle region of an ordered SL, at two different barrier width.

For ordered superlattices, it is possible to observe how the population of electrons inside the wells is confined above the lift-off energy found from the IDOS. It is straightforward to notice that the shape of electron confinement is periodic with the same periodicity of the SL. This quantity integrated over the energy allows to obtain the carrier densities depicted in fig.(3.9). By comparing the two different superlattices, (3.14a and 3.14b), it is possible

to notice the effects of higher confinement in the multiple-QW where the spectral electron density is almost restricted within the wells. The coupling tunneling effects are quite weak and the population in barrier regions is orders of magnitude smaller than the ones in the wells. On the other hand, the device with smaller barriers behaves differently, the maximum value inside the confinement regions is lower and there is a strong coupling between the wells with a not negligible population even in these high potential regions.

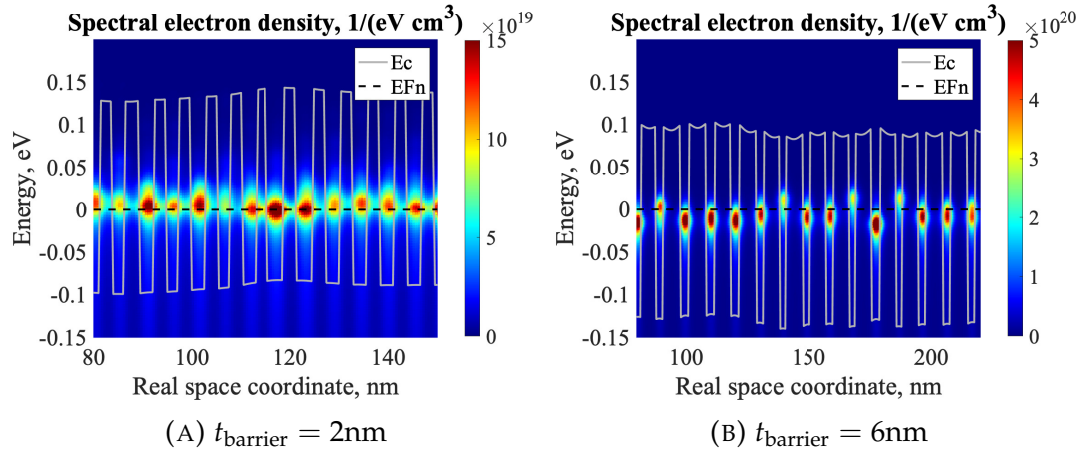


FIGURE 3.15: Electron spectral density depicted for a dozen period in the middle region of an **disorder** SL, at two different barrier width. The colourbar scale is fixed to the one of ordered case.

For disorder superlattices the spectral electron density are depicted in fig.(3.15). Here, it is possible to notice how the disorder changes not only the strength of carrier confinement but also their eigenvalues. This result is very important in describing the differences between order and disorder SL miniband. In those figures is possible to see how the disorder broke the alignment of the confinement state reducing the coupling due to tunneling between the wells. By considering fig.(3.15a), the electron concentration is no longer constant inside the confinement regions, furthermore a change in the width of the wells determine a shift of the ground state energy, a higher width leads to deeper confinement conversely the ground state has higher energy if the well is reduced. Although all this consideration, the disorder is not able to decouple the well because their distances are still small. In fig.(3.15b) due to a lower coupling, the effects of misalignment of ground states are more evident and it further reduces the coupling between the wells.

## Chapter 4

# Out-of-equilibrium simulations

The simulations performed in the previous sections confirm that at equilibrium the landscape potential is able to predict the carrier densities and their region of confinement with good accuracy, just by reshaping the classical potential in an effective way. The best results have been achieved for long geometries (SL) where confined states are quite coupled one to the others. Thereafter, this effective potential has been used to simulate a device out of equilibrium. In chapter 2, it has been explained how it is possible to introduce such potential into a classical Poisson drift-diffusion solver, in which both corrections due to heterostructure and Fermi statistic have been considered. For the following analysis, two superlattices have been taken into the study, both of them have been simulated considering perfect deposition processes and one affected by the positional disorder. Therefore, four different geometries have been simulated out of equilibrium.

For all the devices in the study, a small bias has been applied  $V_{\text{bias}} = 0.1 \text{ V}$  in order to do not further bent the band diagram of the system. Then, results obtained with the landscape potential drift-diffusion solver (LL-PDD) have been compared to the ones obtained with a classical Poisson drift-diffusion (PDD) and with a non-equilibrium Green's function approach (NEGF), with the aim to validate this new model.

Before going on the presentation of results, some consideration on the **carrier mobility** ( $\mu_{(n,p)}$ ) has to be done. In order to perform a PDD electron mobility has to be defined, usually, in a classical implementation, the mobility is chosen equal to the bulk one that is derived from outer models that calculate it by introducing in an effective way different physical effects, as for example scattering. It has been seen that one of the main advantages of the landscape potential is to model a quantum structure as if it was a bulk device, where all the quantum effects are enclosed in this effective potential  $W_C$ . However in order to provide a comparison between the NEGF approach and the LL model the bulk mobility introduced in the LL-PDD model has to be compatible with the description of carriers flow defined in the NEGF approach, where the mobility parameter has not been used at all. In fact, in

the latter model scattering has been introduced through the Büttiker probes defined by the empirical scattering parameter  $\eta$ . It has been seen that this parameter is related to the bulk scattering time  $\tau$  with the relation expressed in eq.(2.53). By knowing  $\tau$  is possible to define a bulk mobility:

$$\mu = q \frac{\tau}{m^*} \quad (4.1)$$

Similarly to what has been done at equilibrium, for all the simulations  $\eta$  has been imposed equal to 10meV leading to a mobility of:

$$\mu_e = 863.93 \text{ cm}^2\text{V}^{-1}\text{s}^{-1} \quad (4.2)$$

This bulk mobility calculated from  $\eta$ , has been introduced in both the classical PDD and in LL-PDD implementations, and it has been considered as constant for the whole device.

The NEGF results have been obtained by introduced in the algorithm the conduction band shape derived with the LL-PDD, and then perform the iterative inner loop in order to find the Büttiker Fermi level that ensures the current conservation.

## 4.1 Superlattice

The first geometry that has been considered is the one depicted in fig.(3.6a), a uniformly doped *n-type* ( $N_D = 10^{18}$ ) superlattice with 31 periods. In this first section of results presentation, this particular geometry has been studied with both perfect periodicity and with the introduction of positional disorder, the two devices have been presented in parallel with the aim to better compare results and understand how the disorder modifies carriers transport.

First of all, the LL-PDD solver has been applied to the equilibrium potential found in the previous simulations. After a few steps, the Newton loop converged providing the wanted outputs. One of them is the potential  $\phi$  that solves the Poisson equation and it can be used to derive and sketch the band diagram of these structures out of equilibrium. In fig.(4.1) is possible to see that for both the devices the difference between the conduction band at the left and right contacts is equal to the bias applied. A small part of the potential drops on the two bulks contacts too, due to the constant doping profile. In the active regions, the potential drops almost linearly from left to right, where the charge effects do not influence the potential. Going into details, by comparing the two band diagram, the one affected by disorder presents

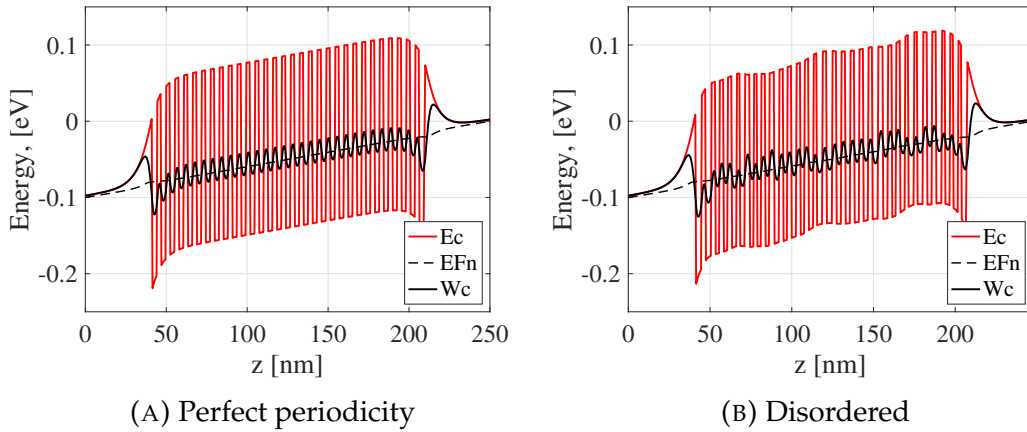


FIGURE 4.1: Out of equilibrium conduction band and its associated effective potential ( $W_C$ ) of a superlattice with barriers thickness equal to  $t_{\text{barrier}} = 2$  nm depicted both with perfect periodic structure and affected by numerical disorder.

an uneven behavior, perfectly followed by the landscape potential. Even out of equilibrium the variation of effective potential between confinement and barriers regions is small meaning that the superlattice is coupled and the miniband is large.

By proceeding on simulations, those conduction bands have been introduced in the NEGF approach and the Fermi level needed for the Büttiker probes has been calculated. The Fermi level  $\mu_{BP}$  has to be defined in such a way the net current through the probes is zero. To do so an inner iterative-method has to be performed as the initial guess of the Fermi level calculated from the LL model has been selected. The above-described procedure is high time demanding due to the high number of mesh point and the numerical derivation of the Jacobian matrix, explained in appendix A. Just to give to the reader a rough idea of the time required to do such simulation, the LL-PDD takes less than 2s to derive all the outputs, while the NEGF takes more than five hours ( $\simeq 2^4$ s) to reach the convergence, so the simulation time saving introduced by the localized potential is huge, with this new landscape method the results are achieved with a time 4 order of magnitude lower than the NEGF.

The comparison between the obtained Büttiker Fermi level and the initial guess is depicted in fig.(4.2). It is important to notice that the new shape of  $\mu_{BP}$  has been found by imposing the boundary condition at the contacts, here the Fermi levels have been set equal to the ones of reservoirs. This new found Fermi level exhibits quite important propriety, that the quasi-Fermi level derived from charge distribution in the LL-PDD does not have. Due to the fact that  $\mu_{BP}$  has been derived from the current density distribution, it has the ability to give an actual representation of how the potential drops between source and drain [19]. The behavior of this curve depends on the conductivity of the device, especially on the one of the active region. It can

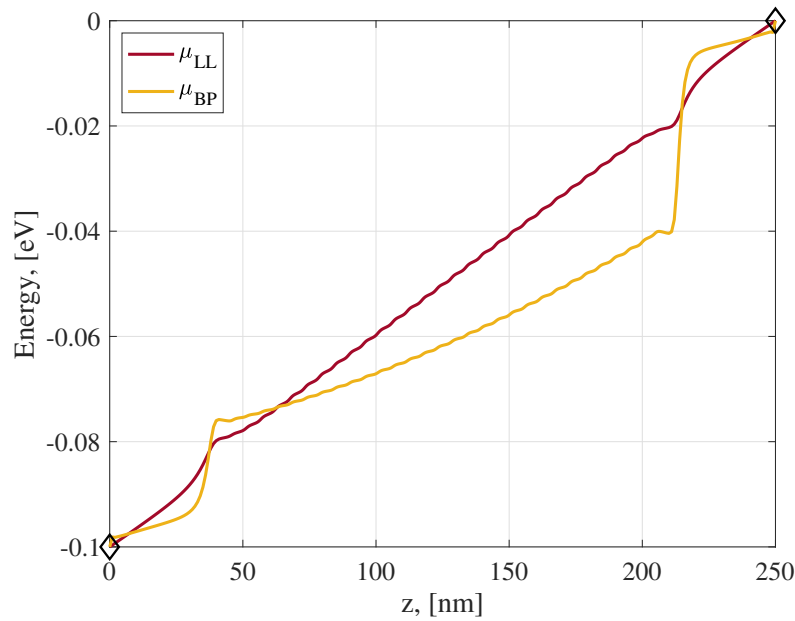


FIGURE 4.2: Quasi-Fermi level (red curve) derived from LL-PDD used as initial guess to derive the Büttiker Fermi level (ochre curve)

be demonstrated that a high conductivity leads to a lower voltage drop in the SL region, leading to a flatter Büttiker Fermi level. The big voltage drops at the two interface between the bulks regions (source and drain) and the active region can be explained considering the contact resistivity at the interface due to charge effects, this interface is strongly out of equilibrium in order to maintain a large current flow. This high resistivity will be the main limitation of current in the device.

Then carrier densities in the active regions found with the three described methods has been compared by limiting the analysis just to the center of the device, where the charge effects are negligible. For ordered and disorder geometry the results are depicted in fig.(4.3).

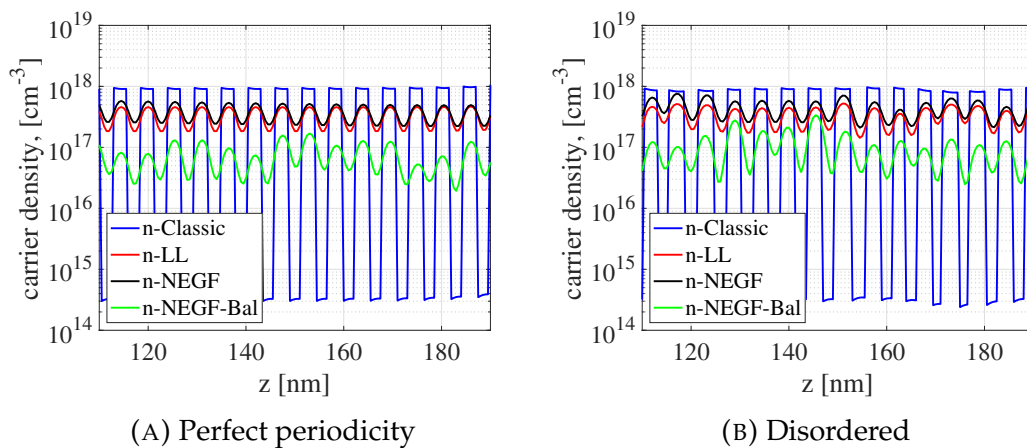


FIGURE 4.3: Electron concentration in conduction band calculated with four different approaches, in an ordered and a disordered superlattice.

In these figures is possible to see how the landscape predictions are still valid out-of-equilibrium matching the outputs of NEGF in a proper way. Going into details, it can be seen that the NEGF approach still slightly overestimates the carrier density due to the broadening of Green's functions. Furthermore, the ballistic ( $\eta = 0$  meV) results are depicted in order to give further proof of the need to introduce the Büttiker probes in order to describe the confinement effects. In fact, as it can be easily seen, the green curve shows an underestimation of carriers values both in the barriers and confinement regions, this is because the lack of Büttiker self-energy does not allow reaching the thermal equilibrium needed to populate the states inside the confinement regions. Finally, even out of equilibrium the classical prediction of carriers totally fails in the description of such geometry.

Before preceding on the comparison of current density between the two models, it is interesting to understand how the disorder affects the shape of the spectral current density, this quantity has been depicted in fig.(4.4).

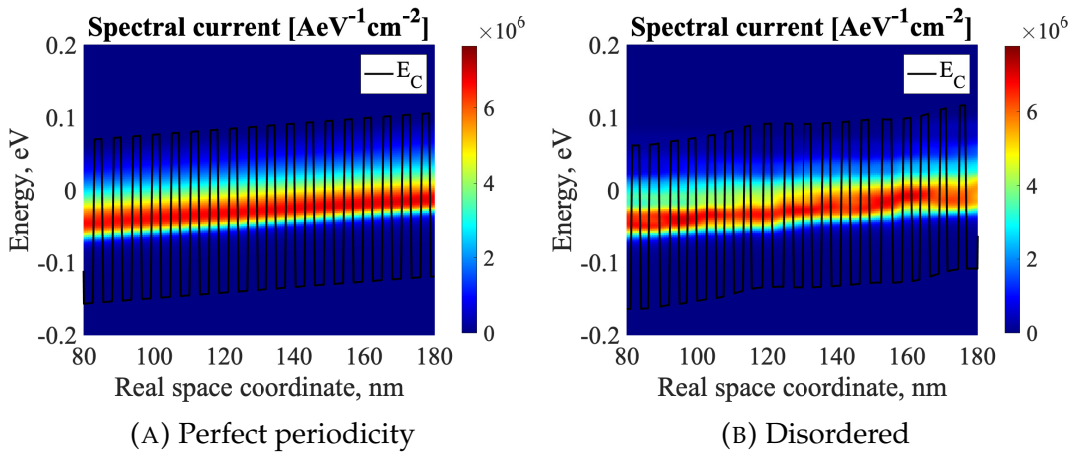


FIGURE 4.4: Electron spectral current density, calculated with NEGF approach for the two cases of SL in study. They are depicted only in a dozen periods leaving unchanged the colour-bar scale and energy axis.

By looking at both graphs it is straightforward to notice that the electron spectral current density is not independent of the spatial coordinate, but the energy spectrum of the current moves downward as points closer to the left contact are considered. The introduction of Büttiker probes in the model breaks the conservation of energy and momenta of the electrons injected from the contacts leaving unaltered their number, so due to thermalization phenomena, the injected electron loses any information about the initial energy leading to asymmetrical current density spectra. By comparing the obtained electron spectral current for a device with perfect periodicity and one affected by positional disorder is possible to see that in the latter case the width of the band, where the transport occurs, depends on the position while is almost constant for the periodic superlattice. This non-uniform shape depends on the alignment of allowed states, in which the electrons have non-null probability to be found. Due to the high coupling between the wells the disorder

does not greatly modify the calculated total current density.

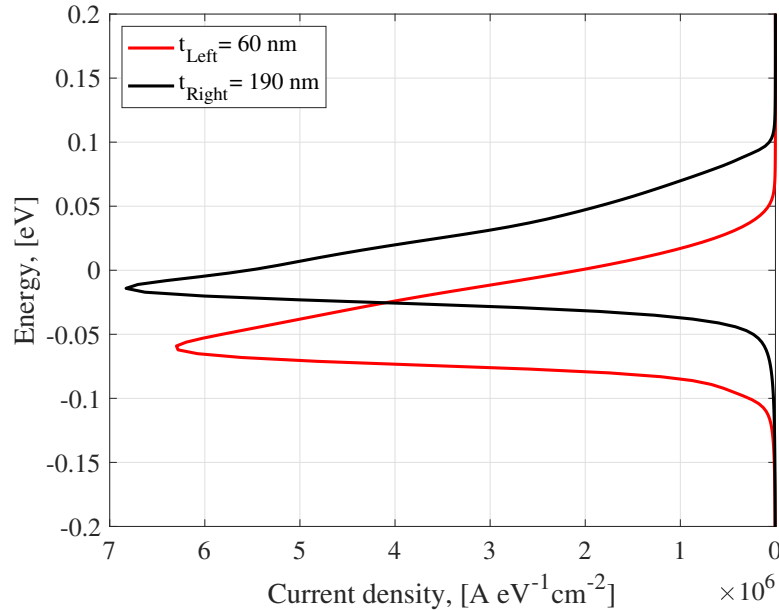


FIGURE 4.5: Cut perpendicular to the  $z$ -axis of the electron spectral current at two different position at the left ( $t_{\text{Left}} = 60$  nm) and right ( $t_{\text{Left}} = 190$  nm) edge of ordered superlattice.

Further proof of the dissipative transport introduced by the Büttiker probes has been done considering the plot in fig.(4.5). Here, only for the order case, a 2-dimensional plot of the spectral electron current has been sketched as function of energy for two different points, the edges of  $x$ -axis depicted in fig.(4.4) equal to  $z_{\text{Left}} = 80$  nm and  $z_{\text{Right}} = 190$  nm. In this graph is possible to notice the two main changes in the spectral current density due to the introduction of Büttiker probes, the first one is that the peak shifts to a lower value of energy by moving from right to left and secondly it reduces its magnitude. This latter effect can be explained by recalling that the divergence of the energy current is equal to the power dissipated due to scattering, [18] and so the energy current decreases in the distance. If a ballistic transport is considered the two curves should be coincident and they do not depend on the spatial coordinate.

Now after having properly described how the electrons flow inside the device within the NEGF approach, the current density obtained from this latter method has been compared to the one calculated with LL and the classical PDD. The obtained result are depicted in fig.(4.6). Here, two different curves are reported for the NEGF procedure: the constant solid curve derives from the integration over energy domain of the previously described electron spectral current density, while the non-constant red dotted curve is the current evaluated at the first loop of the inner iterative NEGF solver, where the Büttiker Fermi level is coincident with the one obtained with the LL-PDD solver, depicted in red in fig.(4.2). Thereafter, it easy to see that the classical

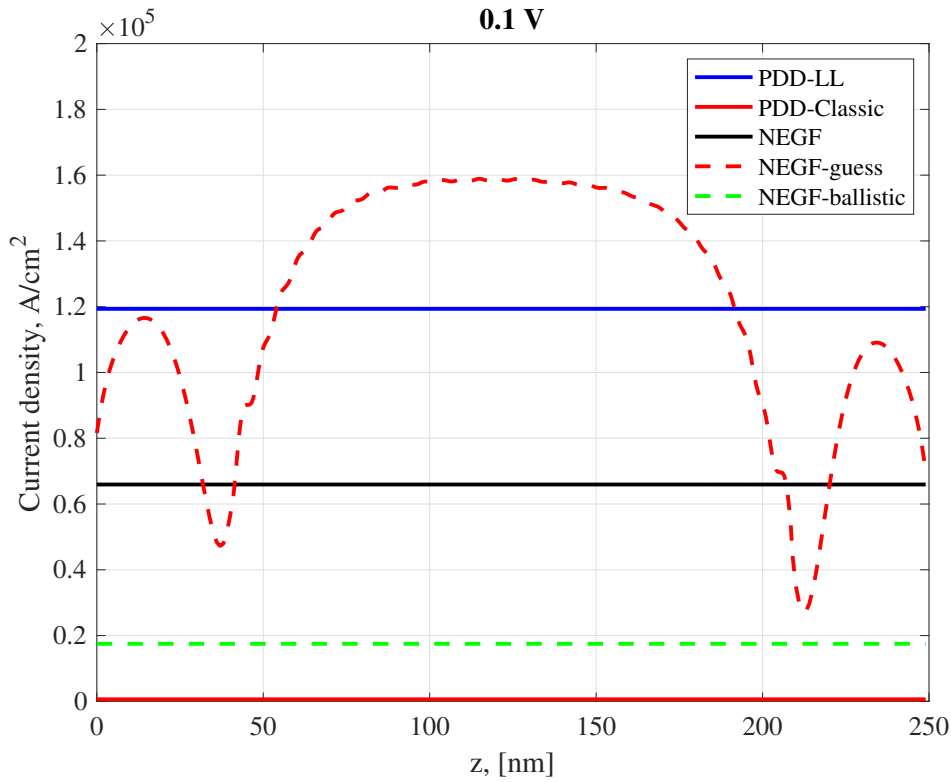


FIGURE 4.6: Current density as function of coordinate  $z$  for the **perfect periodic case**, depicted for all the implemented method.

result extremely underestimates the current because it does not consider the tunneling and quantum effects, indeed the classical prediction is **two order of magnitude** lower than the NEGF one. In this graph also the ballistic current density has been depicted in order to provide a further comparison, as it has been underlined in the description of carriers, the ballistic simulation is able to populate the localized states only with the tunneling of the injected carriers from the contacts, neglecting all the scattering thermalization process. In this geometry, the barriers are quite small and the contribution of tunneling current is not so irrelevant, but it is orders of magnitude lower than the one obtained with the introduction of the scattering. Finally, the blue curve is the results obtained from the LL-PDD model, as expected is constant in the whole device but it slightly overestimates the NEGF one, for this particular geometry the LL prediction is **1.81** time higher than the NEGF.

Following the same scheme of presentation the results for disordered superlattice has been reported in fig.(4.7). Even in this case, the classical calculation is two order of magnitude lower than the NEGF prediction, and as expected does not change in magnitude between the order and disordered case, because the disorder does not change the unconfined states that determine the classical current. The same considerations can be applied to the calculation of ballistic current where, even in this case, its value is not affected by the disorder. Finally, the disorder reduces the value of current calculated with the NEGF and LL approaches, it can be seen that both the

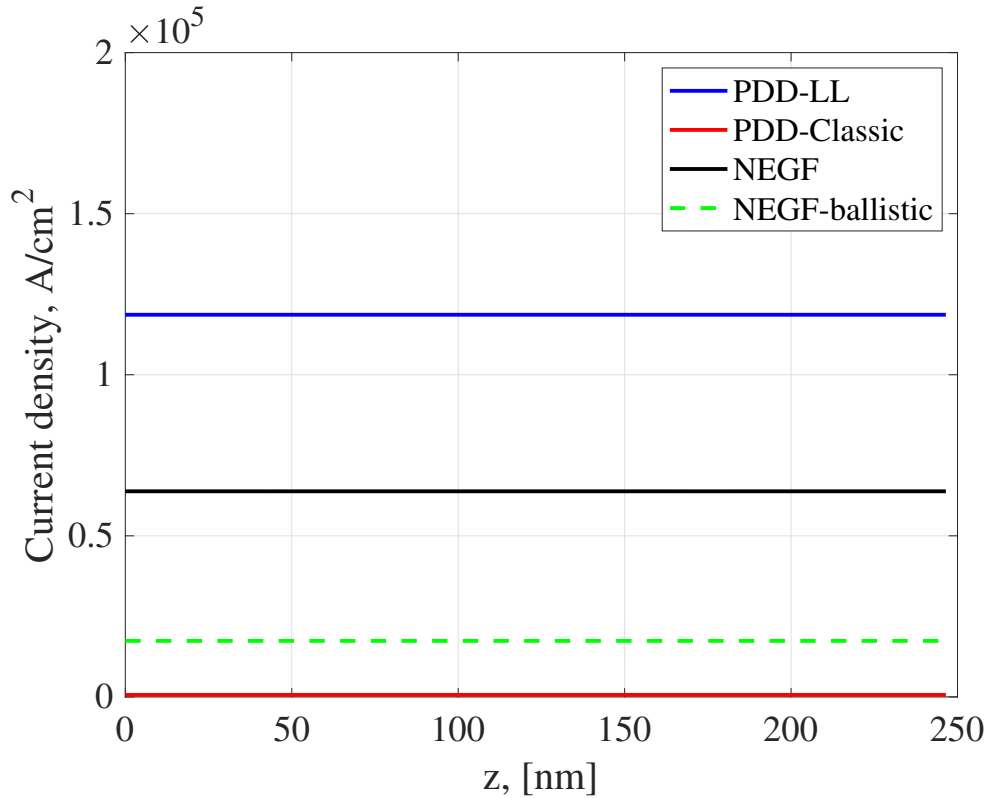


FIGURE 4.7: Current density as function of coordinate  $z$  for the superlattice affected by positional disorder, depicted for all the implemented methods.

constant curves have been shifted to a lower value. As expected, the disorder slightly reduces the flowing of the current within the NEGF approach, this can be explained considering the fig.(4.4b) where the width of miniband is shrunk. The landscape potential has modeled the disorder by changing the shape of effective potential according to the fluctuation of the deposition process, this new effective potential characterized by higher peaks reduce the current. Going into details, the NEGF approach predicts a factor of current decreasing equal to 1.03 while the current calculated form LL-PDD i is less influenced by the disorder, it has been reduced only by 1.01 times.

## 4.2 Multiple-QW

Subsequently, another resistive structure characterized by higher barriers width has been taken into the study, the geometry describes in fig.(3.6c) has been considered. Similarly to the previous section, results have been presented by comparing a perfectly periodic structure and one affected by the positional disorder. On these two devices a bias equal to  $V = 0.1$  V has been applied in order to bring the structure out of equilibrium. All the other parameters such as the mobility or the discretization mesh step have not been modified. Due to the higher length the number of mesh points will be considerably bigger leading to an increasing in the simulation time, the LL model still performs all the simulations steps in time smaller than a few seconds, on the other hand, the NEGF increases drastically the time required to assemble numerically the Jacobian matrix. The total iterative simulation required more than 12 hours.

Following the same style of results presentation used above, the obtained band diagram has been depicted in fig.(4.8).

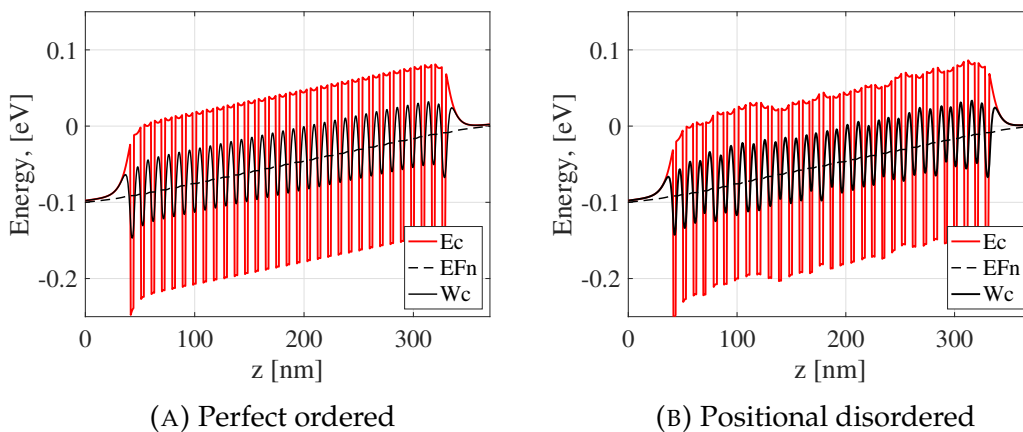


FIGURE 4.8: Out of equilibrium conduction band and its associated effective potential ( $W_C$ ) of a superlattice with barriers thickness equal to  $t_{\text{barrier}} = 6$  nm depicted both with perfect periodic structure and affected by numerical disorder.

Even in those devices, the potential drops linearly in the active regions, and as expected for the not periodic geometry the conduction band edge exhibits an uneven behavior. Furthermore, the effective potential derived with the landscape approach exhibits bigger variation with respect to the high coupled case, because the potential seen by the electron is higher due to the wider barriers.

Then these found potentials have been introduced in the NEGF iterative loop in order to find the Fermi level of the Büttikers probes that ensure the vanishing derivative of the current. For the periodic SL the obtained results have been depicted in fig.(4.9). In this graph is possible to observe that the Fermi level of the Büttiker probes is almost coincident to the ones found with

the iterative LL-PDD procedure, meaning that the motion of carriers is approaching the **diffusive transport** limit.

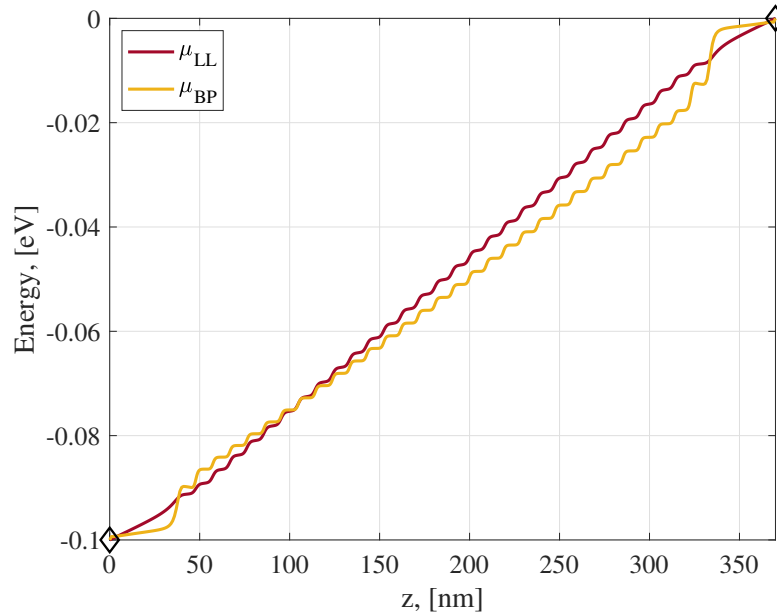


FIGURE 4.9: Quasi-Fermi level (red curve) derived from LL-PDD used as initial guess to derive the Büttiker Fermi level (ochre curve)

Later on, the electron density found with the three different approaches has been depicted in fig.(4.10). Due to the higher effective confined potential, the carrier densities in the barriers are close to the classical prediction, the latter overestimates the results just by only a factor two. For what concerns the landscape and the NEGF approaches, the two curves are very similar for both the simulations with and without the positional disorder. Going into details, as expected the discrepancy between the two models is higher than the previous geometry, this behavior has been observed also at equilibrium, where it has been discussed how the landscape approach behaves better for high coupled superlattices than the low coupled ones. It has to notice that for sake of simplicity the ballistic results have not been depicted.

Presentation of the results continued by depicting the electron spectral current, fig.(4.11), in here it is possible to see that the width of the band where transport occurs is smaller than the previous case. Furthermore, by noting that fig.(4.4) and fig.(4.11) have been depicted with the same colourbar scale, it possible to see that even the maximum value of current density in the central region of the band has been reduced. The cause of these effects is the bigger width of the barriers, which reduces the tunneling current and lowers the coupling strength. As already been stated, if the coupling between wells is low the SL behaves as a set of independent quantum well with eigenstates all at the same energy, as soon as a bias is applied these energy levels shift leading to a very narrow alignment between them. This latter effect is even more visible in the disordered case, fig.(4.11b), where the misalignment due

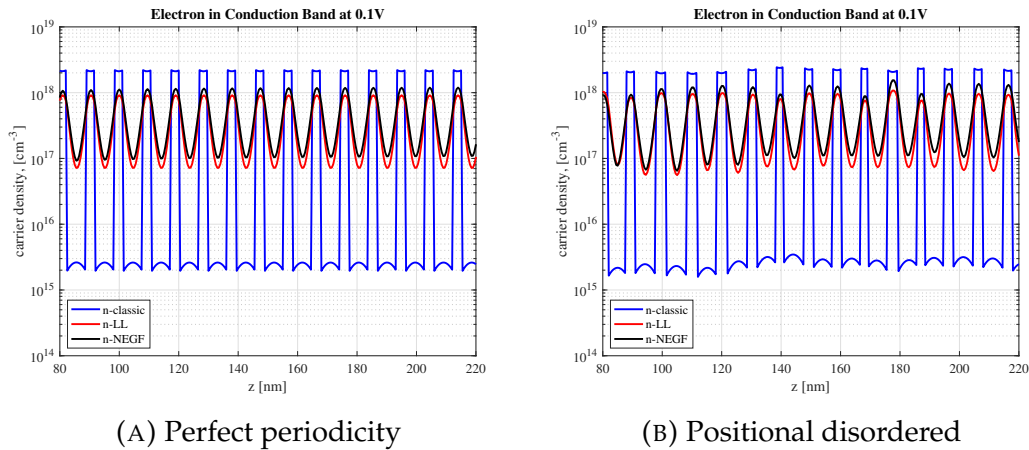


FIGURE 4.10: Electron concentration in conduction band calculated with three different approaches, in an ordered and a disordered superlattice.

to the fluctuation of the layer's width further reduces the tunneling effect between states, leading to an uneven electron spectral current.

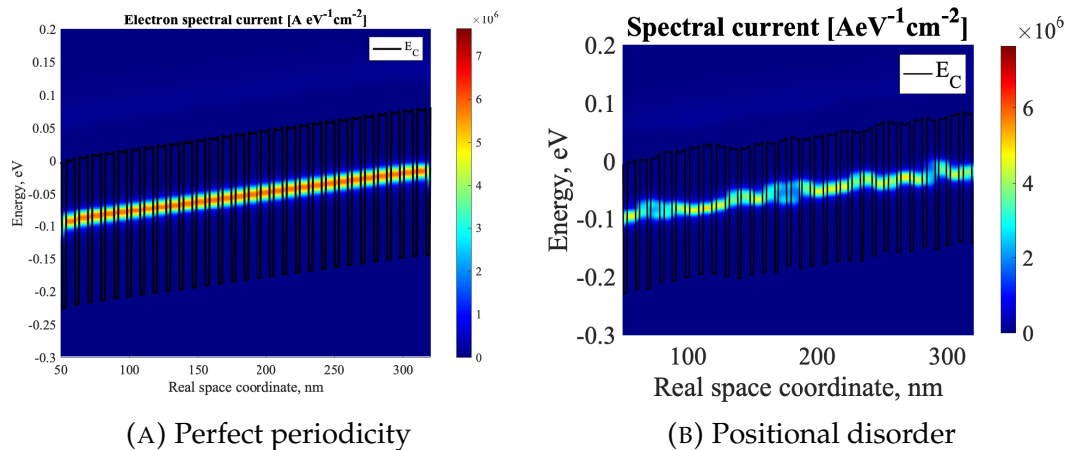


FIGURE 4.11: Electron spectral current density, calculated with NEGF approach for the two cases of SL in study. They are depicted only in a dozen periods leaving unchanged the colourbar scale and energy axis.

Now, just to provide a further comparison, the two-dimensional cut of the electron spectral current at the beginning and at the end of the active region has been depicted in fig.(4.12). Even in this case, the value of the peak decreases by moving from right to left due to dissipative transport. For this device it is also possible to see two more peaks at higher energy, these peaks arise because the not confined electrons flow due to drift at energy higher than the edge of the conduction band. This contribution is not visible in the fig.(4.5) because due to the smaller total length has been shifted to higher value of energy and reduce in magnitude.

Finally, the comparison of the current density has been depicted for both the periodic and disordered SL in fig. (4.13) and fig.(4.14) respectively.

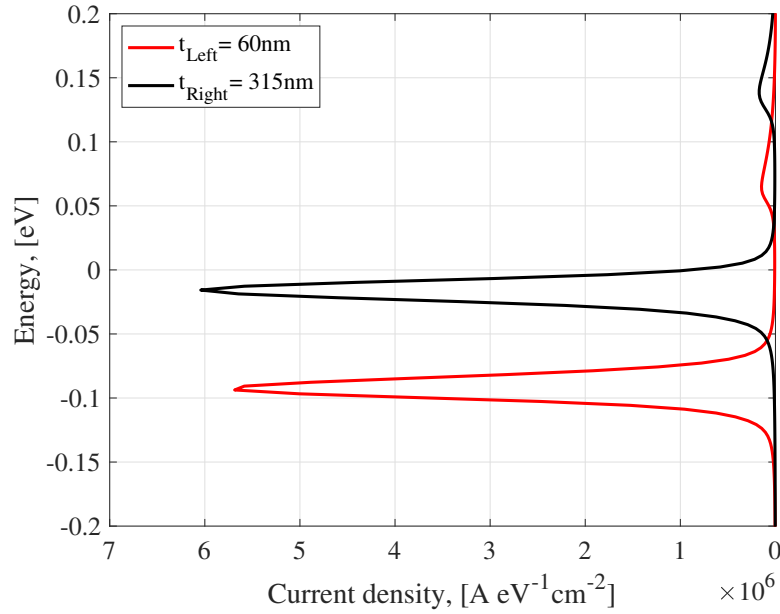


FIGURE 4.12: Cut perpendicular to the  $z$ -axis of the electron spectral current at two different position at the left ( $t_{\text{Left}} = 60\text{nm}$ ) and right ( $t_{\text{Right}} = 315\text{nm}$ ) edge of ordered superlattice.

To start with, the results obtained for the periodic superlattice have been commented and compared to the ones obtained in the previous section. At a first glance, it is possible to notice that even for this device the current density obtained with the landscape method is higher than the one calculated with the NEGF approach, in particular, it is **2.09** time higher, this overestimation factor is bigger in this low coupled SL. Furthermore, it has to notice that the current is smaller w.r.t. the previous case due to the higher width of the barriers and the worst alignment in the states due to poor coupling. The classical prediction is still not able to describe the motion of carriers in such a quantum structure, strongly underestimates the current.

Similarly to the coupled structure, the introduction of disorder does not modify the classical current density because a not uniform periodicity does not change the unconfined carrier's transport. On the other hand, ballistic current behaves differently, in fact in this lower coupled device the ballistic current decreases where a positional disorder is introduced. This can be explained, recalling the fact that in ballistic transport the factor  $\eta$  has been set equal to zero, neglecting the scattering process, hence the carriers can flow toward the active region only by tunneling between the allowed states, introducing the disorder determines a misalignment of these states, leading to a lower tunneling current. No further comment has been done on this effect because is out of the purposes of this thesis.

Moving on, the PDD-LL and the NEGF results have been taken into analysis. As expected even for this superlattice the disorder makes the current decrease for both the LL-PDD and the NEGF simulations, but they model this behavior with a different scaling factor. For what concerns the LL-PDD

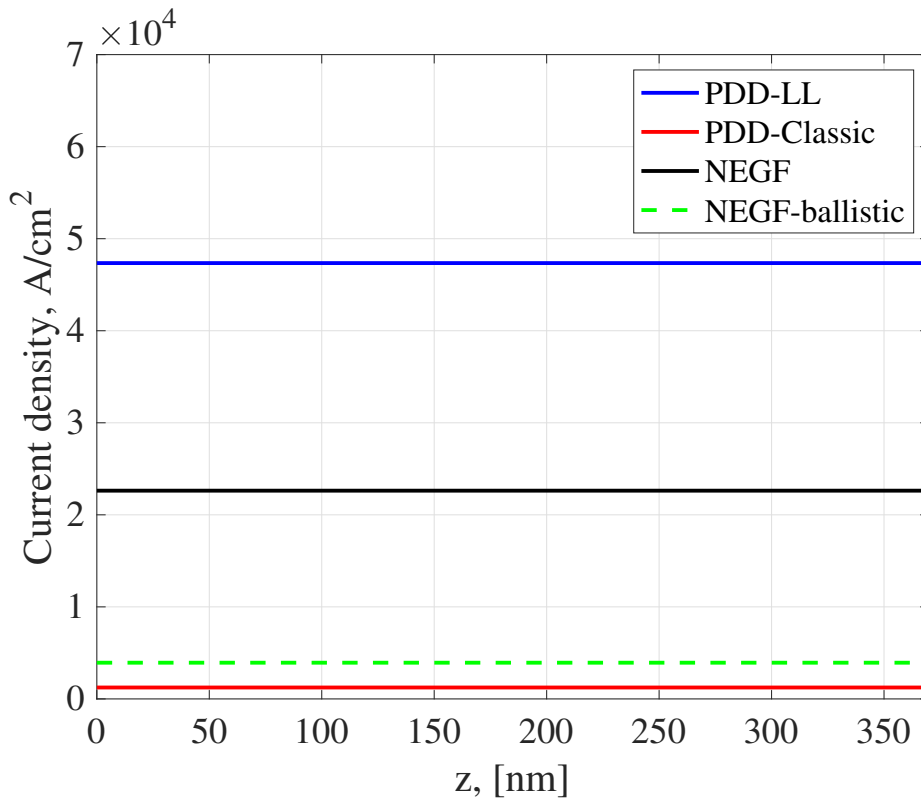


FIGURE 4.13: Current density as function of coordinate  $z$  for the **perfect periodic case**, depicted for all the implemented methods.

current density is 1.03 times smaller while for the NEGF it is 1.24 smaller. Similar to the previously considered superlattice, the reduction of the current due to the disorder is higher in the NEGF approach while the LL-PDD is not able to follow such a change of the current density.

The LL-PDD implements the disorder in the device just by reshaping the effective potential seen by the electrons in the active regions. On the other hand, the NEGF approach, where the scattering has been introduced by means of the Büttiker probes, describes how the carriers, injected and recollected from the reservoirs and from the inner probes, flow within the device, properly describing the transport inside the mini-band. The introduction of disorder breaks the formation of the mini-band, as it can be seen by looking at fig.(4.11b), where a not perfect alignment of the allowed states drastically reduced the current. Unfortunately, this information of the state's alignment can not be introduced inside the landscape potential approach, which, as already stated, can model the disorder just by reshaping the effective potential seen by the carriers, leading to a further overestimation of the current. The above considerations are valid also for the coupled superlattice, where even in that case the reduction in the NEGF approach is higher than the one predicted by LL-PDD even if the discrepancy between the two results is not so high. In this case, instead, the two results are quite different. The main reason for these two behaviors can be understood by recalling the consideration

performed at the equilibrium simulation, for what concerns the coupled SL the degeneracy of state is very poor and the disorder is not able to totally decouple the wells.

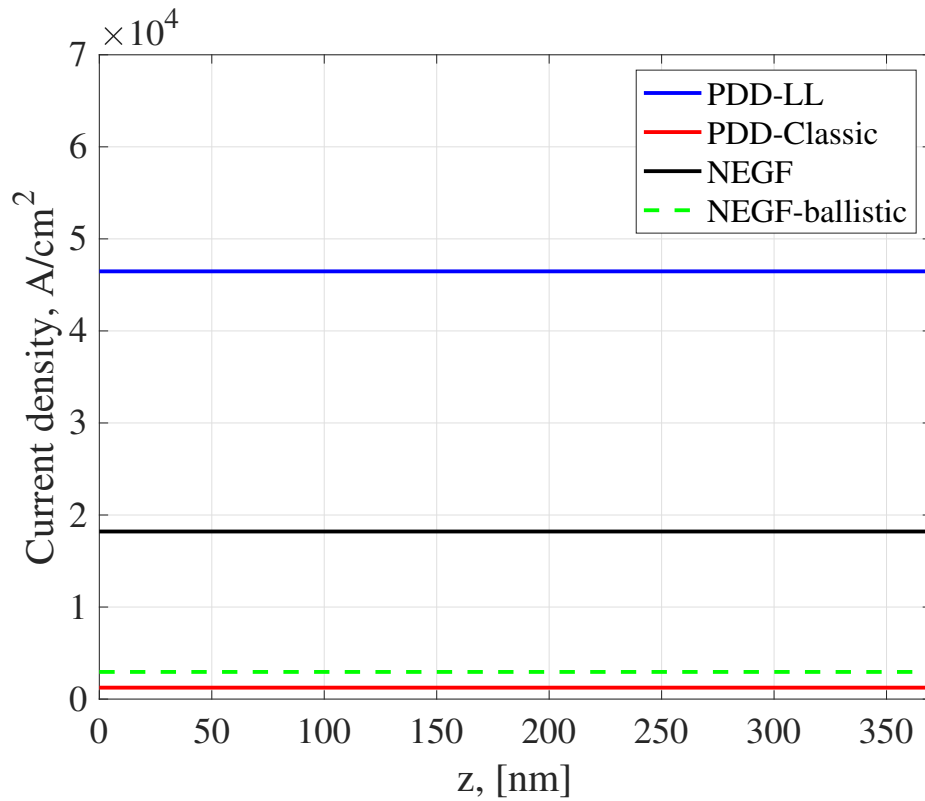


FIGURE 4.14: Current density as function of coordinate  $z$  for the superlattice affected by positional disorder, depicted for all the implemented methods.

## Chapter 5

# Conclusion

In this work, different simulation techniques and models have been applied to several quantum structures in order to provide an exhaustive benchmark for the localized landscape potential. As a first validation check, the localization landscape model was applied to four quantum wells characterized by different confinement potential. For these geometries, carrier densities and integrated density of state have been compared to the ones obtained with both NEGF and Schrödinger models, obtaining a slight underestimation of charge in a confinement region especially for high confined states. Moreover, the ability of LL model to predict the ground state energy has been tested by comparing those results with the ground states found with the Schrödinger equation, obtaining even for this case promising results, unfortunately, the precision of the model is not good enough to properly describe the cut-off energy for a detector, therefore this analysis has dropped off for more complex devices. Then the landscape model has been used with the aim to describe the confinement of carriers in a longer quantum structures, characterized by a higher coupling between the confined states. Even for these geometries, the results have been compared to the ones obtained with the NEGF and Schrödinger approaches. In this study, it has been seen that the landscape model predicts better the carriers confinement for a quite high factor of coupling between the wells. In particular, for high coupled SL the LL theory shows a satisfactory prediction of the density of state and carrier densities, while still slightly underestimate the carriers confinement in the multiple-QW case. Those geometries have been also simulated considering the not perfect periodic case, obtaining promising results.

Subsequently, the superlattices have been simulated with a small applied bias (0.1V), and the outputs have been compared to the ones obtained by the NEGF approach, in which the scattering has been introduced by means of the Büttiker probes. For what concerns the carrier densities and density of state the results are still excellent, on the other hand, the current calculated with the LL approach seems to slightly overestimate the value obtained with the NEGF method. However, the current prediction is far more closer to

the NEGF results than the ones obtained with a classical drift-diffusion approach. It has to recall that the LL current is less than two times bigger than the one found with the NEGF approach, while the classical one is orders of magnitude lower. Finally, even out-of-equilibrium the effect of disorder has been studied too. The landscape model is able to describe the reduction of current due to disorder but, especially for not so coupled quantum well, the reduction factor of current is lower than the ones observed with the NEGF approach.

In conclusion, the main advantage of this theory is the speed, by using this technique for a relative long one-dimensional superlattice the simulation time is 3 order of magnitude lower than a NEGF algorithm out of equilibrium. Moreover, the simulation results show an appealing agreement with the ones obtained with more conventional methods. Further tests of this model can be performed by simulating a more application-oriented type-II superlattice or higher-dimensional devices. By considering the results obtained in this work, it is possible to state that this effective potential properly describes the quantum effects at least for a one-dimensional case and it can be a powerful tool that gives an immediate estimation of the carriers localization and the current density in a quantum structure, without involving high time-consuming algorithms.

## Appendix A

# Numerical evaluation of NEGF

## Jacobian and Broyden iterative

### method

NEGF method needs an iterative procedure that ensure the current conservation within the device, purpose of this iterative procedure is to find the Fermi level of the Büttiker probes for each node defined with the discretization of the space domain.

In this appendix has been depicted how this procedure has been implemented. Regrettably, the derivate of current density along the  $z$  direction, that is the function that has to be minimized, does not explicitly depend on the unknown vector  $\mu_{BP}$ . Consequently, the derivative of the latter formula, with respect to Fermi levels of the probes can not be performed analytically, and so the Jacobian needed fo the Newton method has to be defined in a different way. With the aim to overcome this obstacle the Broyden method has been used, in which as initial guess of the Jacobian a numerical derivation has been performed.

First of all the function that express the derivative of the current density with respect to the coordinate  $z$  has been reported here in eq.(A.1)

$$\mathbf{f}(\mu) = \frac{\partial J}{\partial z} = \Re \left[ \frac{\Delta E}{2\pi} \sum_j \frac{2q}{\hbar} (H \cdot G(E_j)^< - G(E_j)^< \cdot H)_{(i,i)} \right] \quad (\text{A.1})$$

This function has been implemented in the MATLAB code in order to determine numerically the value of current derivative for each node, as a function of Fermi level ( $\mu_{BP}$ ). This function takes the shapes of Fermi level

defined at each node as input and produces the vector  $\mathbf{f}(\mu_{BP})$  as output, in order to ensure the current conservation, this vector has to be theoretically imposed equal to zero, but for this implementation is enough to impose its norm smaller than a certain threshold. In order to resolve this non linear system the Broyden method has been introduced.

The **Broyden method** in numerical analysis is a quasi-Newton method that allows to find the roots of a function  $\mathbf{f}$ . Differently from the Newton's method, that calculate from scratch the Jacobian matrix at each iteration's step, this quasi-Newton's method computes the whole Jacobian only at the first iteration and then updates it with a procedure based on the secant equation. Hence, this new iterative procedure does not totally remove the tricky calculation of the Jacobian but it only limits it to the first step of the algorithm.

Hence, before going on the description of the Broyden's method, the computational steps performed to find numerically the Jacobian has been described. Form definition the **Jacobian** of a vector-valued function in several variables is the matrix of all its first-order partial derivatives. Given a function  $\mathbf{f}: \mathbb{R}^n \rightarrow \mathbb{R}^n$  such that any of its first-order partial derivatives exist on  $\mathbb{R}^n$ , its Jacobian ( $\mathbf{J}$ ) is defined as a square matrix  $n \times n$  written as:

$$\mathbf{J} = \begin{bmatrix} \frac{\partial f_1(\mathbf{x})}{\partial x_1} & \dots & \frac{\partial f_1(\mathbf{x})}{\partial x_n} \\ \vdots & \ddots & \vdots \\ \frac{\partial f_n(\mathbf{x})}{\partial x_1} & \dots & \frac{\partial f_n(\mathbf{x})}{\partial x_n} \end{bmatrix} \quad (\text{A.2})$$

The underscore of function  $\mathbf{f}$  indicates at which node the derivative of the function with respect to the variable  $x_n$  is calculated. In order to be able to determine this matrix for the eq.(A.1), definition of numerical partial derivative for more than one variable has been introduced.

For a generic function  $\mathbf{f}$  derivable in the whole domain, it is possible to express the partial derivative with respect to the variable  $x_i$  as:

$$\frac{\partial f(\mathbf{x})}{\partial x_i} = \frac{f(x_1, x_2, \dots, x_i + \Delta_i, \dots, x_n) - f(x_1, x_2, \dots, x_i, \dots, x_n)}{\Delta_i} \quad (\text{A.3})$$

Where  $\Delta_i$  is a fixed positive small number different from zero. The eq.(A.3)

provides a vector quantity that is equal to the  $i$ -th column of Jacobian matrix defined in eq.(A.2), to fill the whole matrix this procedure has to be performed  $N$  times, where  $N$  is the number of nodes.

```

1 delta = (1e-13)*q; %increment to compute the numerical
  Jacobian [J]
2 [NEGF] = f_NEGF(muN,muL,muR,zvet,Evet,Ec,meffn,T,
  eta,0,mm,dd);
3 rvet =NEGF.eDivCurrent;
4 Jmat = sparse(nn,nn);
5 % Start from the muN at the previou iteration
6 muN_inc = muN*ones(1,nn);
7 % The numerical Jacobian is obtained, one by one,
  the elements of muN,
8 % computing; stored in matrix just to enable using
  MATLAB parallel
9 % toolbox to speed-up computations
10 for indJ = 1:nn
11     muN_inc(indJ,indJ) = muN_inc(indJ,indJ)+delta;
12 end
13 % Parallel for loop: each worker (thread) computes
  a different column
14 parfor ind=1:nn
15     % Computing NEGF with ind-th element with
  relative increase delta
16     [NEGF] = f_NEGF(muN_inc(:,ind),muL,muR,zvet,
  Evet,Ec,meffn,T,eta,0,mm,dd);
17     rvet_inc = NEGF.eDivCurrent;
18     % Computing the ind-th column of the numerical
  Jacobian
19     Jmat(:,ind) = (rvet_inc-rvet)./(delta);
20 end
21 % Enforcing boundry conditions: muN(1) = muL, muN(
  end) = muR
22 Jmat(1,:) = 0; Jmat(1,1) = q;
23 Jmat(end,:) = 0; Jmat(end,end) = q;
24 rvet([1,end]) = 0;

```

FIGURE A.1: MATLAB implementation for the numerical definition of the Jacobian

Returning to the NEGF problem, how this numerical definition of the Jacobian can be introduced in the NEGF implementation? A solution is to use the formula describe in eq.(A.3) where the function  $f$  is one defined in eq.(A.1) and the vector of variable  $x$  is the initial guess of Fermi-level found from the LL-PDD iterative procedure. By doing so, the NEGF solver has to be called  $N$ -times, for  $N$  different Fermi-level shapes, in order to built the initial guess of the Jacobian. The absolute increment ( $\Delta$ ) used to compute the

numerical Jacobian has been set equal to  $10^{-13}$  eV and the MATLAB function `parfor`, that allows to execute loop iterations in parallel, has been used to speed up the calculations.

In fig.(A.1) a section of the implemented MATLAB code has been reported in order to make those comments more accessible to an interested reader. Function `f_NEGF` is the main script for the NEGF approach that gives as an output a **structure** where all the physical quantities in interest is enclosed, as for example the current density (`NEGF.eDivCurrent`). It is possible to see how the function `parfor` has been used in such a way that all the numerical evaluation of the columns of Jacobian are done in parallel. Then the boundary condition has been enforced because the Fermi levels at the contact are fixed and equal to the ones of the reservoirs.

Now that the initial guess of the Jacobian matrix has been calculated, the Broyden algorithm can be introduced to update both the solution and the Jacobian matrix. By following the approach depicted in sec.(1.3) of [22], it is possible to states that knowing both the residual vector and the Jacobian matrix at the  $k$ -th iteration is possible to predict the Jacobian matrix at the  $(k+1)$ -th iteration by the following formula:

$$\mathbf{J}^{k+1} = \mathbf{J}^k + \frac{(\mathbf{y} - \mathbf{J}^k \cdot \Delta x) \cdot \Delta x^T}{\|\Delta x\|} \quad (\text{A.4})$$

where

$$\mathbf{y} = \mathbf{f}(\mathbf{x}^k) - \mathbf{f}(\mathbf{x}^{k-1}) \quad (\text{A.5})$$

and  $\Delta x$  is the update of the solution found with  $\mathbf{J}^k$

Now, by having select an initial estimate of the Fermi level  $\mu_{BP}^0 \in \mathbb{R}^n$  and determine the initial guess of the Jacobian ( $\mathbf{J}^0$ ) by the procedure described above, it is possible to define the Broyden algorithm; by setting  $k = 0$  and repeat the following sequence of steps until  $\|\mathbf{f}\| < \text{tolerance}$  it reads as:

1.  $\Delta\mu = -\mathbf{f}(\mu_{BP}^k) / \mathbf{J}^k$
2.  $\mu_{BP}^{k+1} = \mu_{BP}^k + \Delta\mu$
3.  $\mathbf{y}^k = \mathbf{f}(\mu_{BP}^{k+1}) - \mathbf{f}(\mu_{BP}^k)$
4.  $\mathbf{J}^{k+1} = \mathbf{J}^k + ((\mathbf{y} - \mathbf{J}^k \cdot \Delta x) \cdot \Delta\mu^T) / (\|\Delta\mu\|)$
5.  $k = k + 1$

A possible implementation of this algorithm in MATLAB framework has been reported in fig.(A.2).

The Broyden algorithm introduce a huge time saving in the NEGF method. In this implementation the time consuming NEGF solver is used just one time for iteration, while if the Jacobian has to be defined from stretch the NEGF

solver is called N-times for each iteration. This procedure becomes computational impossible for long devices or for ones with a fine mesh step. For all the simulations that involve the NEGF approach the Broyden algorithm has been used, the main limitation to this implementation is still the numerical definition of the initial guess of Jacobian which practically constitutes the totality of the simulation time.

```

1 while iter<dd.iterMax && (norm(Delta_muN)/q)>dd.
    tolInNEGF
2     [R,C] = dgsequ(Jmat);
3     Jmat_bal = R*Jmat*C;      % balanced Jacobian
4     res = norm(R*rvet);      % residual
5     % Solving the system
6     Delta_muN = - C*(Jmat_bal\(R*rvet));
7     % Updating the solution
8     muN1 = muN + Delta_muN;
9     [NEGF] = f_NEGF(muN1,muL,muR,zvet,Evet,Ec,meffn,T,
        eta,0,mm,dd);
10    rvet1 = NEGF.eDivCurrent;
11    rvet1([1,end]) = 0;
12    % Updating the Jacobian
13    y = rvet1-rvet;
14    delta_J = ((y-Jmat*Delta_muN)*Delta_muN')/(
        Delta_muN'*Delta_muN);
15    Jmat = Jmat + delta_J;
16    Jmat = sparse(Jmat);
17    % B.C.
18    Jmat(1,:) = 0;    Jmat(1,1) = q;
19    Jmat(end,:) = 0;    Jmat(end,end) = q;
20    %
21    rvet = rvet1; muN = muN1;
22    iter = iter+1;
23    if (norm(Delta_muN)/q)<dd.tolInNEGF
24
25        disp('----- Converged!-----');
26
27    end
28 end

```

FIGURE A.2: MATLAB implementation of Broyden method for the iterative problem of minimization of derivative current density.



# Bibliography

- [1] J. Rothman, E. De Borniol, P. Ballet, *et. al.*. *HgCdTe APD-focal plane array performance at DEFIR.* , Proc. SPIE 7298, Infrared Technology and Applications XXXV, 729835, 6 May 2009.
- [2] Elena A. Plis, *InAs/GaSb Type-II Superlattice Detectors.* Center for High Technology Materials, Department of Electrical and Computer Engineering, University of New Mexico, Albuquerque, USA , 10 April 2014.
- [3] K. Bandara, J. Choe, W. Francombe, M. Perera, A. Lin. *GaAs/AlGaAs superlattice miniband detector with 14.5  $\mu\text{m}$  peak response.* , , Applied Physics Letters. 60. 3022 - 3024, 1992.
- [4] C. Asplund, H. Martijn, IR nova. *IR detection using type-II superlattice photodiodes.* May 2013.
- [5] A. J. Steckla, P. Chen. *GaAs quantum well distributed Bragg reflection laser with AlGaAs/GaAs superlattice gratings fabricated by focused ion beam mixing.*, Department of Electrical and Computer Engineering, University of Cincinnati, April 1995.
- [6] D. Bohm. *A Suggested Interpretation of the Quantum Theory in Terms of "Hidden" Variables. I.* January 1952.
- [7] M. Filoche, S. Mayboroda, *Universal mechanism for Anderson and weak localization.* University of Bristol, Bristol, United Kingdom, July 20, 2012.
- [8] M. Filoche, M. Piccardo, Y.-Renn Wu, Chi-Kang Li, C. Weisbuch, S. Mayboroda, *Localization landscape theory of disorder in semiconductors I: Theory and modeling.* University of Bristol, Bristol, United Kingdom, April 18, 2017.
- [9] T. Tsai, K. Michalczewski, P. Martyniuk, C. Wu, Y. Wu. *Application of localization landscape theory and the  $k \cdot p$  model for direct modelling of carrier transport in a type II superlattice InAs/InAsSb photoconductor system.* J. Appl. Phys. 127 , 033104, 2020
- [10] C. Weisbuch, S. Nakamura, Y. Wu and J. Speck, *Disorder effects in nitride semiconductors: impact on fundamental and device properties,* November, 2020
- [11] S. Datta, *Quantum Transport: Atom to Transistor,* Cambridge University Press, 2005

- [12] A. Tibaldi *Physic-base modeling of semiconductor device*. Lecture Notes, February 2020.
- [13] F. Bertazzi, M. Goano. *Modeling carrier transport in nanoscale devices*. Lecture Notes, October 2019.
- [14] D. Arnold *Effective Confining Potential of Quantum States in Disordered Media*, PHYSICAL REVIEW LETTERS, February 2016
- [15] S. Subramanian, *A self-consistent solution of one-dimensional Schrodinger-poisson equation by Newton-Raphson iteration technique*, Oregon State University
- [16] A. Tibaldi, F. Bertazzi and M. Goano, *Simulation of electronic devices at thermodynamic equilibrium CAD of semiconductor devices*. Lecture Notes, October 2019.
- [17] M. Filoche, M. Piccardo, Y.-Renn Wu, Chi-Kang Li, C. Weisbuch S. Mayboroda, *Localization landscape theory of disorder in semiconductors III: Application to carrier transport and recombination in light emitting diodes*. University of Bristol, Bristol, United Kingdom, April 20, 2017.
- [18] S. Datta, *Nanoscale device modelling: the Green's function method*, School of Electrical and Computer Engineering, Purdue University, July 24, 2000
- [19] R. Venugopal, M. Paulsson, S. Goasguen, S. Datta, and M. S. Lundstrom, *A simple quantum mechanical treatment of scattering in nanoscale transistors*, January 31, 2003
- [20] K. Wang, R. Grassi, Y. Chu, S. H. Sureshbabu, J. Geng, P. Sarangapani, X. Guo, M. Townsend, and T. Kubis *Introduction of multi-particle Büttiker probes-Bridging the gap between drift diffusion and quantum transport*, July 02, 2020
- [21] T. Kubis, P. Vogl. *Assessment of approximations in nonequilibrium Green's function theory*, May 05, 2011
- [22] B.A. van de Rotten. *A limited memory Broyden method to solve high-dimensional systems of nonlinear equations*, October 20, 1976